ALEXANDRE GUERREIRO FONSECA

Licenciado em Ciências de Engenharia de Micro e Nanotecnologia

PEROVSKITE SOLAR CELLS: DEVELOPING A SIMPLE, FAST AND LOW-COST FABRICATION TECHNOLOGY

Dissertação para obtenção do Grau de Mestre em Engenharia de Micro e Nanotecnologias

Orientador: Professora Doutora Elvira Fortunato, Professora Catedrática, Departamento de Ciências dos Materiais, Faculdade de Ciências e Tecnologias da Universidade Nova de Lisboa

Co-orientador: Manuel João de Moura Dias Mendes, Marie Curie Post-Doc Fellow, Departamento de Ciências dos Materiais, Faculdade de Ciências e Tecnologias da Universidade Nova de Lisboa

Júri:

Presidente: Prof. Doutor Rodrigo Martins
Arguente: Prof. Doutora Maria Alexandra Barreiros
Vogal: Prof. Doutor Manuel João Mendes

FACULDADE DE CIÊNCIAS E TECNOLOGIA
UNIVERSIDADE NOVA DE LISBOA

Outubro 2017

“O que sabemos é uma gota; o que ignoramos é um oceano.”

– Isaac Newton

Perovskite Solar Cells: Developing a simple, fast and low-cost Fabrication Technology

Acknowledgements

Gostaria de agradecer a todos que de certa forma contribuíram para o meu sucesso nestes últimos 5 anos mais importantes da minha jornada como estudante.

Em primeiro lugar gostaria de agradecer a ambos Prof. Dra. Elvira Fortunato e ao Prof. Dr. Rodrigo Martins por abrirem e manterem as portas abertas a todos os estudantes que queiram seguir a área de Micro e Nanotecnologia, uma vez que sem o seu esforço continuo esta oportunidade era impossível, e também pelas excelentes condições de trabalho proporcionadas. Em especial atenção agradeço à minha orientadora, Prof. Dra. Elvira Fortunato, pela oportunidade de explorar um tema tao recente e interessante, e também ao meu co-orientador, Prof. Manuel Mendes que tanto chateei e que tanto me ajudou e aconselhou ao longo da realização deste trabalho.

Um outro grande agradecimento não poderia deixar de ser feito à já Mestre Carolina Fidalgo Marques com quem pude partilhar todos os momentos stressantes e por ser a única a compreende-los, e também ao Eduardo Duarte que mesmo antes de iniciar o seu trabalho me ajudou na realização de muitas das células solares produzidas.

Agradeço também a toda a equipa do cenimat: Sónia Pereira, Alexandra Gonçalves, Rita Branquinho, Emanuel Carlos, Daniela Gomes, Ana Rovisco, Olalla Sanchez, Tiago Mateus, Joana Pinto e Tomás Calmeiro pela ajuda em todas as minhas dúvidas e competência na realização de algumas das etapas importantes neste trabalho.

Gostaria de agradecer também a todos os meus amigos que me acompanharam nesta etapa com especial atenção ao João Coroa (a Donzela) de entre muitas coisas por ter aturado a minha pior ressaca (‼), Tiago Gameiro (Tiggus), Shiv Bhudia, Luís Oliveira, Vasco Santos, Viorel Dubceac, Inês Martins, pelos estudos intermináveis e dormidas hilariantes em minha casa pós festas e por fim e especialmente, ao Marco Moreira por todas as dormidas em minha casa, treinos na residência, noites de riso, desabafo, conversas e estudo intermináveis, e ao Pedro Trigo por me animar mesmo quando nada o podia fazer, por todas as cacetadas nos jogos de futebol e especialmente por estar sempre preocupado com a saúde dos meus rins. Também a todos os outros, apesar de não serem aqui mencionados, deixo o meu sincero agradecimento.

O maior dos Obrigados não poderia de deixar de dedicar aos meus pais galinhas, José e Teresa, que para além de 23 anos a aturar o seu filho rabugento (Guru Maldisposto) sempre me apoiaram. Sem eles era impossível ter chegado onde cheguei. Nunca esquecendo também os meus irmãos Susana e Frederico!

Por ultimo gostaria também de deixar um Grande agradecimento à minha namorada Alexandra que esteve e aturou todos os meus bons e maus momentos, foi também por vezes a minha fotografa de serviço e revisora de muitos dos erros que eu cometia na escrita.

Um muito Obrigado a todos!

Abstract

Solar energy is the most abundant renewable resource and is regarded as the most promising for the sustainability of our society. Perovskites are a class of semiconductor materials with unique properties since they allow films fabrication with high electronic quality using non-vacuum solution techniques. Therefore, such materials are interesting for a wide range of opto-electronic applications. Perovskites allow rapid, simple and low-cost solar cell manufacturing, being nowadays considered the most promising material to compete with silicon in photovoltaics technology. However, the production of homogeneous $MAPbI_3$ films by Spin Coating is challenging, as it requires precise control of several factors that influence the films' properties. In this work, the influence of the main deposition parameters on the $MAPbI_3$ thin films manufacture was studied to find the best processing conditions that enable obtaining films as homogeneous and uniform as possible. This allowed attaining $MAPbI_3$ polycrystalline films with state-of-art quality, having grain sizes between 3 and 13 μm and UV-Visible absorption of 85-90 %. The remaining layers (i.e. selective contacts) of the Perovskite cell structure were investigated as well, allowing the fabrication of sets of full solar cells with a maximum V_{OC} of 0.77 V and J_{SC} of 7.65 $mA.cm^{-2}$.

Keywords: Photovoltaics, Perovskite Solar Cells, Spin Coating, Polycrystalline Thin Films, Selective Contacts

Resumo

A energia solar é o recurso renovável mais abundante e é considerada a mais promissora para a sustentabilidade da sociedade. As perovskites são uma classe de materiais semicondutores com propriedades únicas que permitem o fabrico de filmes com alta qualidade eletrónica usando técnicas por solução sem necessidade de vácuo. Assim, tais materiais são interessantes para uma vasta gama de aplicações optoelectrónicas. Perovskites permitem também uma fabricação rápida, muito simples e de baixo custo, de células solares, sendo, hoje em dia, considerado o material mais promissor a competir com a tecnologia do silício. Contudo, a produção de filmes homogéneos de $MAPbI_3$, por *Spin Coating,* é um desafio, exigindo um controlo preciso dos fatores que influenciam a sua morfologia. Neste trabalho foi estudada a influencia de vários passos inerentes à deposição filmes finos de $MAPbI_3$, a fim de encontrar as melhores condições de processamento que permitem a obtenção de filmes o mais homogéneos e uniformes possível. Foram obtidos filmes finos de $MAPbI_3$ com qualidade semelhante à literatura, com obtenção de tamanho de grãos entre os 3 e os 13 µm e absorções médias de ≈ 85-90 % na região do visível. Foram também estudas as camadas seletivas da estrutura das células solares que permitiram a fabricação de conjuntos das mesmas com obtenção de um V_{OC} máximos de 0,770 V e um J_{SC} de 7,65 $mA.cm^{-2}$.

Palavras-chave: Fotovoltaico, Células Solares de Perovskite, *Spin Coating*, Filmes Finos Policristalinos, Contactos Seletivos

Abbreviations

AFM – Atomic Force Microscopy

CuSCN – Copper(I) Thiocyanate

DMF – N,N-dimethylformamide

DMSO – Dimethyl Sulfoxide

FTO – Fluorine-doped tin oxide

EDS – Energy Dispersive Spectrometry

ETL – Electron Transport Layer

EtOH – Absolute Ethanol

HTL – Hole transport Layer

IPA – 2-propanol

LI-TSFI – Bis(trifluoromethane)sulfonimide – Lithium salt

MA – Methylammonium

MAI – Methylammonium Iodide

$MAPbI_3$ – Methylammonium Lead Iodide

PbI_2 – Lead iodide

PCE – Power Conversion Efficiency

PSC – Perovskite Solar Cells

Rms – Root mean square

Rpm – rotations per minute

SEM – Scanning Electron Microscopy

Spiro-MeOTAD - 2,2',7,7'-tetrakis(N,N-di-p-meth-oxyphenylamine)-9',9'-spirobifluorene

TCO – Transparent Conducting Oxide

TiO_2 – Titanium dioxide

TTPI - Titanium Isopropoxide

UV – Ultraviolet

Uv-Vis – Ultraviolet-Visible

XRD – X-ray Diffraction

ZAD – Zinc Acetate Dihydrate

ZnO – Zinc Oxide

Symbols

cm – centimeter

E_g – Optical bandgap

E_{ph} – Photon energy

FF – Fill Factor

h – hour

I – Iodine

I_{SC} – Short circuit current

J_{SC} – Short circuit current density

M – Molar concentration

min – Minute

mL – milliliter

mm – millimeter

Pb – Lead

R_P – Parallel resistance

R_S – Series resistance

R_{SH} – Shunt resistance

s – Second

°C – Degrees Celsius

Ω – ohm

µL – microliter

µm – micrometer

V – Voltage

V_{OC} – Open circuit voltage

η – Efficiency

Table of Contents

List of Figures

List of Tables

Motivation and Objectives

There are many types of energy sources available for use in a wide range of applications. However, most of them are difficult to obtain involving harmful processes to the environment, i.e. are non-renewable energies and very pollutant.

Research on renewable energy fields has been growing, targeting both innovative ways of collecting and transforming the available energies and new ways to increase energy efficiency, thus requiring a detailed study in the materials science field. Among the set of renewable energies, solar energy has a great potential because the surface of the Earth receives in one hour the total amount of energy consumed by all human activities in a year. Therefore, the use of this type of energy can be not only enough for human demands, but can also allow reducing substantially the CO_2 ambient emissions. [1, 2] Besides, sunlight is one of the main and most abundant clean energy sources and one of the most searched.

Nevertheless, the generation of solar electricity via photovoltaic (PV) technology requires a huge breakthrough concerning the development of new materials and techniques, with the purpose of increasing efficiency and yield combined with low-cost, simplicity and speed fabrication factors. Silicon is currently the material mostly used in solar cells fabrication. However, this material implies a huge amount of costs, starting from its extraction and treatment to the solar cells fabrication itself. In this way, Perovskite solar cells (PSC) became a promising alternative since they have unique properties and the ability to be processed by a wide range of fabrication techniques that do not need high vacuum systems or high temperature. Therefore, Perovskite-based PV enables simple, fast and low-cost solar cells fabrication.

This work aims mostly to study the influence of different spin coating fabrication steps, as is the Perovskite precursor solution concentration, annealing temperature, amount of non-coordination solvents, the type of substrate and substrate pre-heating temperature, and solvent (DMF:DMSO, N,N-dimethylformamide: Dimethyl Sulfoxide) ratio on perovskite thin films morphology, to reach the best conditions for solar cells performance. Besides optimizing the Perovskite film, we also developed the other layers of the cell structures, namely the selective contacts to improve charge collection.

Work strategy

The realization of this work was divided in three main phases:

1. ETL (Electron Transport Layer) and HTL (Hole Transport Layer) fabrication and optimization, using the conventional solutions and studying the thickness influence on the transmittance spectrum, by varying the rotation speed of the spinner and the number of depositions. To study the crystallinity, XRD measurements were performed.

2. Optimization of the perovskite layer, studying the influence of the perovskite solution concentration, annealing temperature, amount of non-coordination solvents (chlorobenzene/toluene), the type of substrate, deposition solution/substrate temperature and DMF:DMSO ratio on morphology and grains size. SEM images, XRD and absorbance spectra analysis were performed.

3. Solar cells fabrication and characterization, where acetate masks were fabricated, via laser cut, to deposit the contacts and fabricate complete solar cell structures. Using a Sun Simulator, the photovoltaic response was characterized and the main solar cells parameters were calculated. UV-Vis spectroscopy, SEM and EDS were performed to characterize the full cell structure morphology and composition, while the layer thicknesses were measured by cross section SEM images.

Chapter I: Introduction

1. Solar Cells: Materials and Operation

Solar energy is one of the main and most abundant clean energy sources, which also has the least impact on the environment, deserving a special dedication. Solar to electrical energy conversion is a phenomenon denominated photovoltaic effect, which was discovered by Alexandre Becquerel and later explained by the Einstein photoelectric effect. [3]

Solar cells are the basic unit of the solar energy conversion devices and their operation is based on the photovoltaic effect. Generally, solar to electric energy conversion in solar cells occurs in three main steps, as illustrated by Figure 1: sunlight absorption, with electron-hole pairs formation, if $E_{ph} \geq E_g$, electron-hole pairs separation into free electric charges and, finally, the free charges derive to the positive and negative contacts (negative charge to the negative contact and positive charge to the positive contact), through which they access the external circuit.

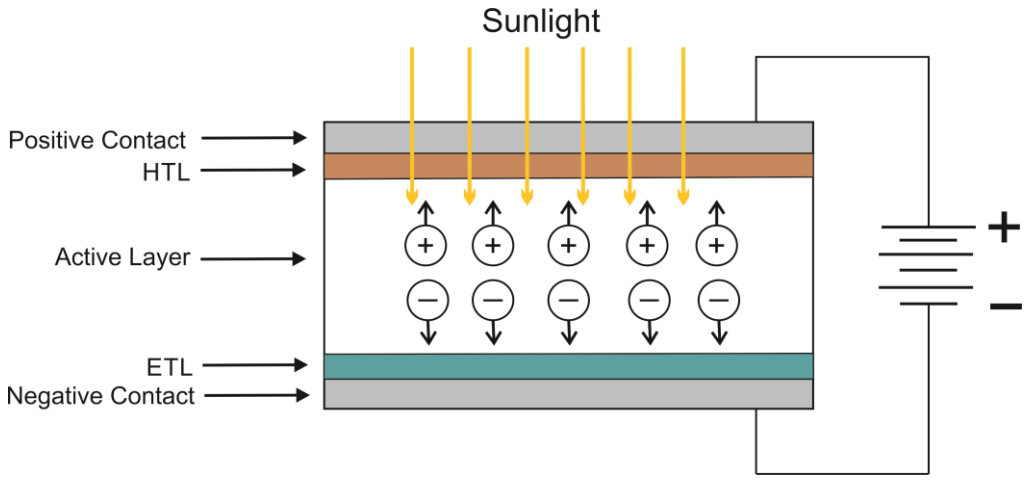

Figure 1: Basic solar cell operation principle representation.

The efficiency with which all these events occur depends mainly on the materials choice and its features as the band gap, absorption coefficient, carrier mobility, photosensitivity, etc. In addition, for thin film technology is important to achieve high uniformities, homogeneities and very good interfaces to minimize the losses mechanisms, especially by recombination. The combination of these features influences the solar cells performance which can be characterized by: I_{SC} and I_{mp} (short-circuit current and current at maximum power point), V_{OC} and V_{mp} (open-circuit Voltage and Voltage at maximum power point), FF (Fill Factor), P_{Max} (maximum Power), η (efficiency), R_S (series Resistance) and R_P (parallel Resistance). All of these parameters can be calculated through the solar cells IV curve using the equations presented in **section 1 of Appendices**.

In this way, for a material to be applied on solar cells technology, it must have adequate semiconductor properties as high photosensitivity, high absorption coefficient, ability to transport electrons and holes and, especially a band gap as close as possible to the ideal 1.34 eV, in case of single junction solar cells, for a maximum energy conversion of 33.7 % (Shockley-Queisser limit).[4] Besides that, it is advantageous to allow fast and easy fabrication, at low costs and low temperatures. However, some of these specifications are very dependent on the final application.

Thin-film solar cells are made from a large variety of semiconductors including amorphous and polycrystalline Si, GaAs, CdTe and $CuInSe_2$, as well as organic semiconductors. [5] However, many of these materials are too toxic (e.g. CdTe), too expensive (e.g. GaAs), rare and do not allow low costs and low temperatures solar cells fabrication. Thus, inorganic–organic lead halide perovskite materials appear particularly promising for single junction solar cells technologies replacement.

2. Perovskite Solar Cells

Perovskite is a class of semiconductor materials with unique properties as tunable bandgap, high absorption coefficient, high absorption over visible spectrum, ambipolar charge transport with high carrier mobility and long charge diffusion lengths, which make it a promising material for photovoltaic and optoelectronic applications. [6-10] The crystal structure has a generic ABX_3 formula, illustrated by Figure 2, where A is an organic or inorganic (or a mix of both) cation (methylammonium (MA - $CH_3NH_3^+$); formamidinium (FA - $CH_3(NH_2)_2^+$); cesium (Cs^+)) is selected to balance total charge, B is a divalent metal or a mix of divalent metals (Pb^{2+}; Sn^{2+}; Ge^{2+}), and X an anion (Cl^-; Br^-; I^-) or a combination of anions, which can crystalize into cubic, tetragonal and orthorhombic phase depending on the annealing temperature. [6, 8], [10-13]

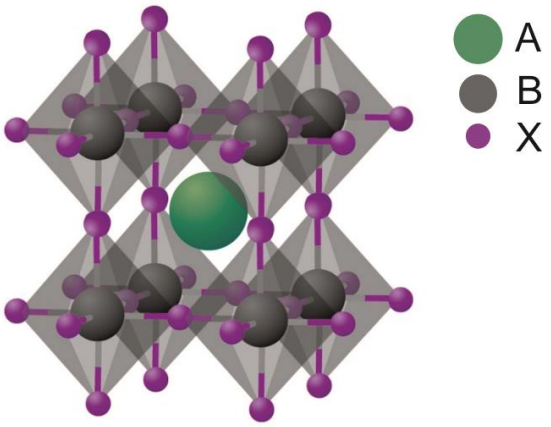

Figure 2: Crystal structure of cubic metal halide perovskites with the generic chemical formula ABX_3. [14]

This semiconductor material works as a PV active layer, being able to convert sunlight into electric current and transport electron and hole carriers with different efficiencies depending on its composition. As already extensively studied, a composition change on perovskite structure regarding anions and/or cations allows, depending also on stoichiometry, different optical, electrical and structural properties, as different band gaps, crystalline orientation, morphologies and uniformities, grain sizes, and even better humidity stabilities, due to different anion-cation interaction which lead to changes in crystallographic arrangements. [6, 10, 15]

Perovskite thin films can be processed using a large range of techniques as one and two-step spin coating, chemical vapor deposition, inkjet printing, dip coating, thermal evaporation, spray pyrolysis, atomic layer deposition, blade-coating, among others, and even a mix of techniques. [6, 7, 9], [16 – 23] However, the high lead toxicity and the perovskite instability to moisture and UV radiation are the main issues of these semiconductors. Despite these significant disadvantages, Perovskite PV appears to be promising for a new solar cells generation, since high efficiency (> 20 %) and large-scale production is possible at low temperatures, high fabrication rates and particularly at very low costs.

2.1. Influence of different factors on perovskite films thickness, morphology and crystallization

In thin films technology, high morphological uniformities, high crystallinity levels and high overall surface coverages are essential conditions for good solar cell performance. In this way, many efforts were made to enhance and optimize these factors, especially for the spin coating method, and suggestions were hypothesized in order to better understand the perovskite behavior and reach the best processing conditions.

Giles E. Esperon et al. was a pioneer, studying distinct factors affecting perovskite thin film coverages and morphologies and their influence on the solar cells performance. In his study, it was observed lower coverages as the annealing temperature and time increases, by formation of large perovskite islands over a compact TiO_2 layer. Besides these factors, it was also observed a film

coverage enhancement with initial higher perovskite thicknesses and with higher compact TiO_2 thicknesses, still without efficiency improvement due to the increase in series resistance(thus, charge collection decrease).[9] The same observation was made by Amalie Dualeh et al. regarding the annealing temperature, for perovskite thin films over mesoporous TiO_2, and it was hypothesized a crystal growth from a large number of nucleation sites with consequent smaller island formation, for lower annealing temperatures. Despite the morphological analysis, they also performed XRD measurements in which was observed incomplete crystallizations, regardless of annealing time, for temperatures below 80 °C and perovskite properties degradation for temperatures above 120 °C with the appearance of PbI_2. The presence of this undesired compound changes the film properties, leading to a yellow film color, higher band gap and corresponding XRD peaks. [24]

Motivated for reaching high surface coverages and high morphological quality, M. Xiao and co-workers reported an interesting and efficient spin coating approach, named Fast Deposition-Crystallization (FDC). Just by dropping a non-coordination solvent (in which $CH_3NH_3PbI_3$ has a low solubility and which increase the speed of nucleation process by removing the excess of perovskite precursor solutions solvents) such as chlorobenzene, toluene, chloroform, among others, it was obtained full surface coverages and high uniform perovskite thin films. [25] Later, W. Nie et al. reported a hot casting approach, in which precursor solution and substrate were heated at a certain temperature before the spin coating step, reaching also full surface coverages and a remarkable millimeter grain scale. [26] Despite being two different approaches, both can be explained by the fast crystallization of perovskite upon exposure to solvents where it has a low solubility. Those two studies were a very important advance twoards high perovskite solar cells efficiencies, proving its dependence on surface coverage, film morphology and grain size.

Regarding the precursor solutions, other factors were reported having a critic influence on the final films appearance. As is intuitive, solution concentration has a great influence on films thickness, which increases with the concentration due to the higher viscosities and amount of material. Despite that, perovskite precursor solutions can be prepared using distinct solvents, as DMF, DMSO, GBL, among others, with different properties (e.g. viscosities, densities and boiling points) and, therefore, giving distinct properties to the final solution. In this way, N. Jeon et al. and B. Cai et al. studied the influence of such solvents and reported bad film coverages with pinholes formation using a single solvent and, more importantly, a MAI-PbI_2-DMSO complex formation, when using DMSO, as a critical phenomenon on perovskite crystallization. As such, it was hypothesized that this complex retards the fast interaction between MAI and PbI_2 during the DMF or GBL evaporation, which ones exhibits higher evaporation rates than DMSO and in which $CH_3NH_3PbI_3$ has a high solubility. [7, 27] However, despite the desired slow interaction between MAI and PbI_2 during the DMF or GBL evaporation, it is extremely important a fast crystallization into a $MAPbI_3$ crystals due to the organic cation hydroscopic nature. [28]

Another example is the precursor solution aging time, studied recently by H. Tsai. In this case, the simple fact of a perovskite thin film produced using precursor solution with different stirring times, left at 70 °C, induces significant grain size changes, reaching hundreds of microns. Based on LaMer diagram, it was hypothesized that the formation of larger nucleation seeds within the precursor solution, combined with hot casting method, generates high morphological quality and, especially, high grain size, essential to reduce grain boundaries and trap states. [29]

In a nutshell, all these studies demonstrate the importance of thin films surface coverage, morphology, grain size and crystallization on solar cells performances, but, actually, other factors, regarding the charge collection optimization may be very helpful for even higher efficiencies. An example is the optimum layer thickness considering not only the charges diffusion length but also the absorption coefficient to achieve maximum broadband absorption in the full visible spectrum range. Another example is the selective layers application, i.e, the deposition of an electron transport layer (ETL) and a hole transport layer (HTL) which allow lower recombination rates since they are able to transport electrons and reject holes and vice versa, respectively. In this way, the charge collection is more efficient and the overall performance is improved.

2.2. Electron and Hole Transport Layer

One of the great advantages of perovskite semiconductors is their ambipolar charge transport. As was reported by Henry J. Snaith et al., perovskite thin films reach charge diffusion lengths > 1 µm, enough for highly efficient charge collection without any additional selective layer, which can be tuned using different perovskite compositions. [30] However, it is possible to achieve higher efficiencies with the application of specific electron (ETL) and hole (HTL) transport layers attached to the corresponding n/p contacts, decreasing the recombination rate. Besides, such layers may mitigate short circuits situations in case of bad perovskite uniformity with the existence of pinholes in the perovskite film.

These layers are mainly constituted by semiconductor materials with higher band gap than the active layer, since they should not absorb much light, having either a high electron (ETL) or hole (HTL) affinity. Besides transparency, the choice of such layers is also based on the band alignment, i.e, based on the conduction band alignment for the ETL case and the valence band alignment for the HTL case, in order to avoid Schottky junctions, as illustrated by Figure 3:

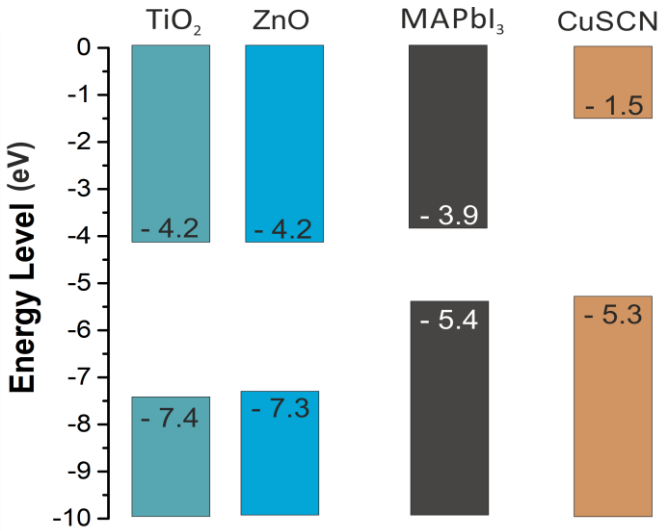

Figure 3: Perovskite, TiO_2, ZnO and CuSCN energy levels with respect to the vacuum level and respective band alignment (values based on reference [31]*).*

In the ETL case, many materials were tested including TiO_2, ZnO, PCBM. [32 – 38] TiO_2 is the most used material for both planar and mesoporous solar cell configurations. However, ZnO is a good candidate to replace TiO_2 due to its appropriate bandgap (≈ 3.3 eV), high electron mobility (35 $cm^2V^{-1}s^{-1}$ for pure ZnO, [39], compared to 0.1 $cm^2V^{-1}s^{-1}$ for anatase TiO_2, [40]) and higher transparency. [36, 41]

There are two conventional Perovskite solar cell architectures based on the ETL configuration: planar heterojunction (Figure 4 b)), in which the ETL is a compact ultra-thin (≈ 20-60 nm) film, and mesoscopic architecture (Figure 4 a)) in which the ETL thickness is higher (≈ 100 nm) and the perovskite film is soaked in a mesoporous matrix. The use of a mesoporous TiO_2 scaffold is reported to strongly attenuate the hysteresis effects and increase dramatically the carrier-collection efficiency. Thus, the advantage of the mesoscopic over the planar configuration is that it can reach carrier-collection efficiencies close to 100 %, even when the charge carrier diffusion length is much shorter than the photon absorption length. [14]

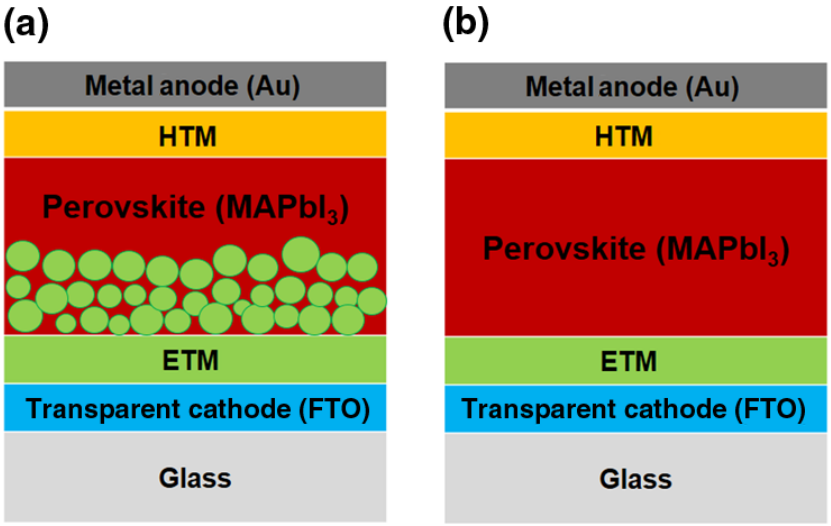

Figure 4: a) Mesoscopic and b) Planar solar cells architectures illustrations. (Adapted form reference [42])

Concerning the HTL case, the highest efficiencies were obtained using the organic Spiro-OMeTAD semiconductor. However, its high cost makes it not viable for large scale solar cell fabrication. In this way, CuSCN appears to be a good substitute because it presents dramatically higher hole mobility of approximately 0.01 - 0.1 $cm^2V^{-1}s^{-1}$ (as compared to 4×10^{-5} $cm^2V^{-1}s^{-1}$ in Spiro-OMeTAD), high optical transparencies and favorable energy levels (E_{VB} = - 5.3 eV and E_{CB} = - 1.5 eV). [43, 44] Besides, it is relatively cheap, thermally stable, it doesn't require high annealing temperatures (≈ 90 °C) and it was already used by many researchers with efficiencies > 10 %. [43 – 46] In addition, as M. Jung et al. discussed, inorganic semiconductors used as HTL may prevent degradation by humidity. [43]

3. Spin Coating

The perovskite high deposition versatility is an important advantage over many other materials used in solar cells technology. Although vacuum-assisted thin film deposition techniques allow better film and interfaces quality, spin coating is the most common method since it does not need vacuum systems, which imply very high costs, and is a simple, low cost and low time consuming method. Wet coating also enables deposition of a wider range of semiconductors, where film thickness is mostly controlled by the rotation speed of the spinner and by the solutions viscosity/concentration.

For perovskite deposition, spin coating technique showed to be a quite favorable method, specially the solvent-induced fast crystallization-deposition approach, studied by M. Xiao and coworkers. This method, adopted by many researchers, induces a highly uniform and flat perovskite thin film with high grain sizes, just by dropping a non-coordination solvent on the spin coating final instants, essential for high charge transport quality and preventing losses, as previously mentioned. [25]

Chapter II: Experimental

1. Device fabrication

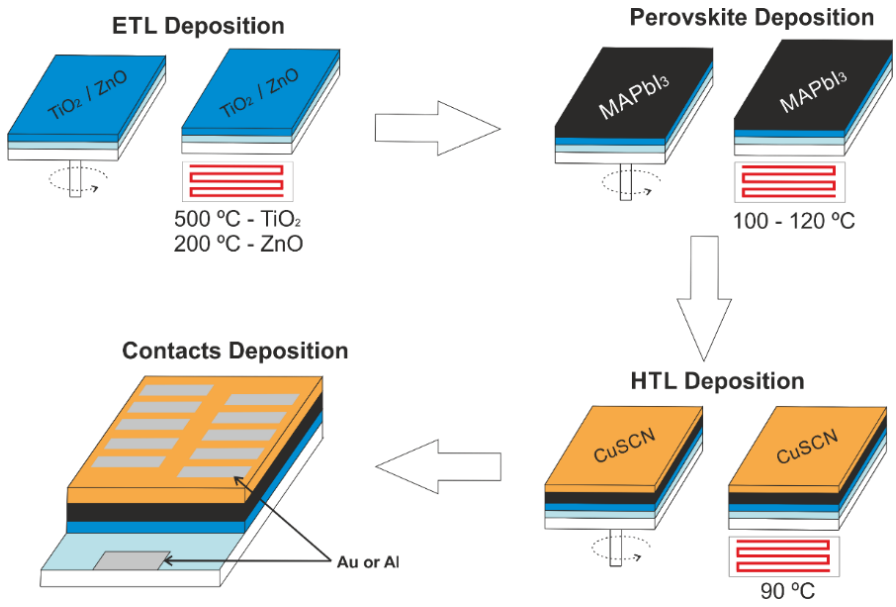

Figure 5: Solar cells fabrication scheme.

The solar cells fabrication can be defined by 4 main processes, as illustrated by Figure 5: electron transport layer (ETL) deposition, active layer (perovskite) deposition, hole transport layer (HTL) deposition and, finally, back and front contacts deposition. All processes are carried out by spin coating, except the contacts depositions, as described in detail below. The used materials information is presented in Table 9.

1.1. Substrate preparation and ETL deposition

Fluorine doped tin oxide (FTO) coated glass slide (100 mm x 100 mm x 2.2 mm, 13 Ω/sq, 82-84.5% transmittance), purchased from *SIGMA ALDRICH*, and glass without any TCO coating (100 mm x 100 mm x 1 mm), cut into 2.5 cm × 2.5 cm, were cleaned by sonication in IPA and deionized in water, for 15 min each, after a detergent rub. Then the substrates were dried with nitrogen and, finally, cleaned with UV ozone treatment for 15 min.

For the ELT, to study the TiO_2 and ZnO compact layer thickness, the precursor solutions were deposited on glass without any TCO coating via spin coating, for 30 s at 3000 and 6000 rpm and 2000 and 6000 rpm, respectively, with a ramp of 2000 $rpm.s^{-1}$, dried at 120 °C for 5 min and sintered at 450 °C – 500 °C and 200 °C, respectively, for 30 min. In order to estimate the thickness per deposition, it was varied the number of sequential depositions, with a drying step of 120 °C for 5 min between depositions, and sintered at 450 °C – 500 °C. Similarly to these, the CuSCN HTL was deposited at 1000, 2000 and 4000 rpm for 30 s with the same ramp and then annealed at 90 °C for 30 min.

For solar cells fabrication, approximately 30 nm TiO_2 compact layer was deposited on FTO coated glass via spin coating, for 30 s at 6000 rpm with a ramp of 2000 $rpm.s^{-1}$, using the precursor solution 1 from **section 3.1 of Appendices**. After the spin coating, the compact layers were dried at 120 °C for 5 min and then annealed at 450 °C – 500 °C, respectively, for 30 min and left to cool down to room temperature. Similar to the compact layer, the mesoporous TiO_2 layer was deposited by spin coating for 30 s at 6000 rpm with a ramp of 2000 $rpm.s^{-1}$, using the solution 2 from **section 3.1 of Appendices**, and sintered at 450 °C - 500 °C for 30 min.

Li-doping of compact and mesoporous TiO_2 ETL was accomplished by spin coating a solution of Li-TFSI in acetonitrile (solution 3 from **section 3.1 of Appendices**) at 1000 rpm for 10 s and 3000 rpm for 20 s, followed by another sintering step at 450 °C for 30 min, as described elsewhere. [47]

1.2. Perovskite solution preparation and deposition

Before the perovskite deposition, both precursor solution (preparation described in **section 3.3 of Appendices**) and substrates were heated either at 25 °C, 50 °C or 70 °C. Then the solution was spin coated in a two-steps program at 1000 and 6000 rpm for 10 and 20 s respectively, with a ramp of 2000 rpm.s^{-1}, on different substrates (Mesoporous and compact TiO_2, compact ZnO and FTO). During the second step, chlorobenzene and toluene was poured on the spinning substrate prior to the end of the program, with volumes between 80 and 200 µL. The substrates were then annealed at temperatures between 70 ° and 200 °C for 1 h, in ambient air.

1.3. HTL and top electrode deposition

After the perovskite annealing, the substrates were cooled down for few minutes and a CuSCN solution (solution from **section 3.2 of Appendices**) was spin coated at 3000 rpm for 20 s and annealed at 90 °C for 20 min, as described elsewhere [48]. Finally, using acetate masks fabricated by LASER (*Universal LASER Systems)*, 50-80 nm of aluminum/gold top electrode, with an area of 0.8 cm × 0.1 cm, was thermally evaporated under high vacuum, as described elsewhere.

2. Characterization

2.1. UV-Vis Spectrophotometry

The optical characterization of the thin films layers was based on direct transmittance, for ETL and HTL deposited over uncovered glass and FTO coated glass, and also full optical analysis (transmittance, reflectance and absorbance) was acquired by Shimadzu UV 3101PC by obtaining Reflectance and Total Transmittance with a ISR-260 Integrating Sphere within a range of 300-830 nm.

For thickness estimation, optical simulations were performed with the analytical Transfer Matrix Method (TMM) implemented in Mathematica 7.0 (developed by Prof. Manuel Mendes).

2.2. SEM-EDS and AFM

The cross section and surface morphology of complete solar cells and the surface morphology of perovskite thin films were examined by scanning electron microscopy (SEM) using a Carl Zeiss Auriga crossbeam (SEM-FIB) workstation instrument equipped with an Oxford Intruments AZtec X-ray energy dispersive spectrometer and a Tabletop Microscope TM3030 Plus + Quantax 70 SEM, respectively.

The surface topography of the ETL was investigated and analyzed by atomic force microscopy (AFM, Asylum MFP3D).

2.3. XRD

The structural analysis of all thin films layers, TiO_2, ZnO, CuSCN and the full device structure (without back and front contacts) was performed by X-ray diffraction (XRD) using a PANalyticalX'Pert Pro X-ray diffractometer in Bragg–Brentano geometry, with a monochromatic Cu-Kα radiation source (wavelength 1.5406 Å).

Perovskite XRD measurements were carried out from 10° to 90º (2θ) and, for ETL/HTL, grazing mode analysis was carried out with an X ray incident angle of 0.4° from 20° to 90° (2θ) and the spectra analysis was acquired with High Score Plus software (PANalytical).

2.4. Electrical Characterization

IV-characterization was performed in ambient conditions at room temperature under AM1.5 illumination conditions (100 mW.cm^{-2}) with a SS150 Reflective Solar simulator from Sciencetech.

Chapter IV: Results and Discussion

As discussed in the introduction, to reach an efficient perovskite solar cell it is necessary to study and optimize its structure layer by layer. Thus, this chapter presents the main results concerning the morphological, structural, electrical and optical properties of each layer.

1. ETL and HTL Characterization

1.1. XRD characterization

The ETL was the first layer to be optimized since all solar cell structure is built on top of this layer. As described in introduction, the ETL/HTL main objective is to block holes/electrons transport and increase electron/hole collection, respectively, decreasing the carrier recombination and, therefore, increasing the charge collection efficiency. Thus, it is important to reach a high ETL and HTL crystallinity level.

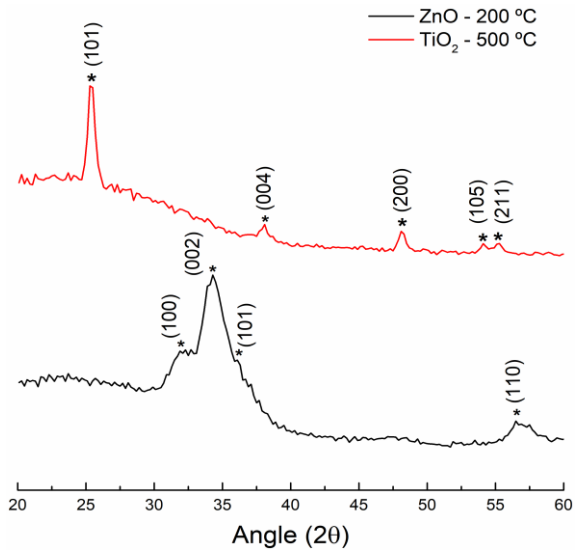

Figure 6: Grazing mode XRD spectra of TiO_2 and ZnO ETLs, and CUSCN HTL, deposited over glass by one-step program spin coating of 6000 rpm (for TiO_2 and ZnO) and 3000 (for CuSCN) for 30 s with 2000 rmp.s^{-1} ramp and a final annealing step of 500 °C, 200 °C and 90 °C, respectively, for 30 min.

Figure 6 shows the XRD results of TiO_2, CuSCN and ZnO thin films, where it is possible to see the presence of (101), (004), (200), (105) and (211) planes, at approximately 25.3° ,38° ,48° ,54° and 55°, respectively, in case of TiO_2, which indicates the presence of tetragonal crystal planes of anatase phase TiO_2. [49], [50] In the CuSCN case, it was observed the presence of (101) and (012) at 27.1° and 30.1°, respectively indicating the presence of rhombohedral β-phase, according with Alex K.-Y. Jen and co-worker results. [51]

Concerning ZnO, it was obtained (100), (002), (101) and (110) planes, at 31.9°, 34.3°, 36.1° and 56.5°, respectively, showing a hexagonal polycrystalline (wurtzite) structure. [52], [53] However, as Yanming Sun and co-workers claim, increasing the annealing temperature reduces the oxygen-deficient component and increases the number of Zn-O bonds and, therefore, the peaks related to (100) and (101) planes may be more defined and intense. [36] However, in this work TiO_2 is the main ETL and, therefore, it was studied only ZnO annealed at 200 °C. In addition, as is revealed in Jianning Ding et al. work, the presence of the (110) plane indicates a film thickness above 20 nm, since for lower thicknesses this peak does not exist. [52]

For these materials, it was calculated the average of crystal size using Scherrer's equation applied to the strongest peak, and the results are summarized in Table 1:

Table 1: Phases and grain size results of HTL (CuSCN) and ETL (TiO_2/ZnO) obtained by XRD measurements.

Material	**Phase**	**2θ**	***Plane***	**FWHMs**	**D (nm)**
TiO_2	Tetragonal (anatase)	25.3°	(101)	0.01082	14.2
ZnO	Hexagonal	34.3°	(002)	0.04537	3.7
CuSCN	Rhombohedral	27.1°	(101)	0.01745	8.9

1.2. Optical characterization

The optical characterization allowed not only to further confirm the presence of such layers but also to study the influence of their thickness in the transmittance spectrum. As such, Figure 7 shows the transmittance spectrum as a function of ETL thickness, for the TiO_2 case, which was controlled by the number of depositions and the rotation speed of the spinner.

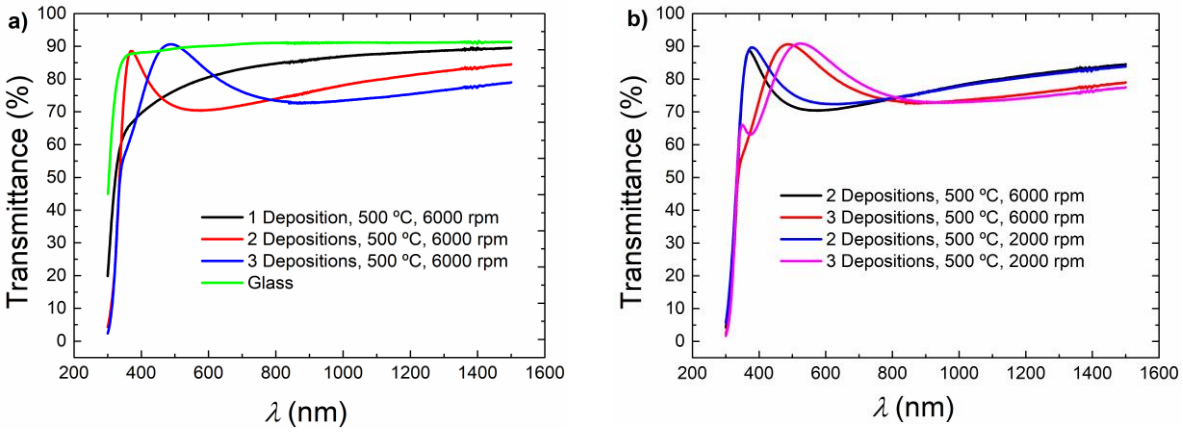

Figure 7: Influence of a) depositions number and b) spinner rotation speed on TiO_2 thin films transmittance spectrum. Depositions accomplished by one-step program spin coating of 2000 rpm and 6000 rpm with a final annealing step of 500 °C for 30 min. Fitting with the TMM analytical program, we determine a thickness average of 32 ± 10 nm per deposition, confirmed by profilometry

Figure 7 a) shows an increase of peaks (interference fringes) number with the number of depositions, which is due to the increase of the TiO_2 film thickness. According with the literature this result is expected and the fringes are a useful tool for thin films thickness estimation. [54] Figure 7 b), reveals an insignificant thickness decrease as the rotation speed increases, however, the film homogeneity improves remarkably going from 2000 to 6000 rpm which is a good result since it prevents short-circuit situations.

Although all factors promote certain shifts of these curves, the number of depositions is what most affects the layer thickness, showing the higher red shift of the interference fringes as the thickness increases. All samples reached a maximum transmittance close to 90 %, which is a good result since the perovskite will be illuminated through this layer.

Using the TMM analytical program and fitting these curves with the simulations, as shown in Figure 35 d) in **section 4 of Appendices**, it was possible to determine a thickness average of **32 ± 10 nm per deposition**, confirmed by profilometry (average of 3 measurements per sample).

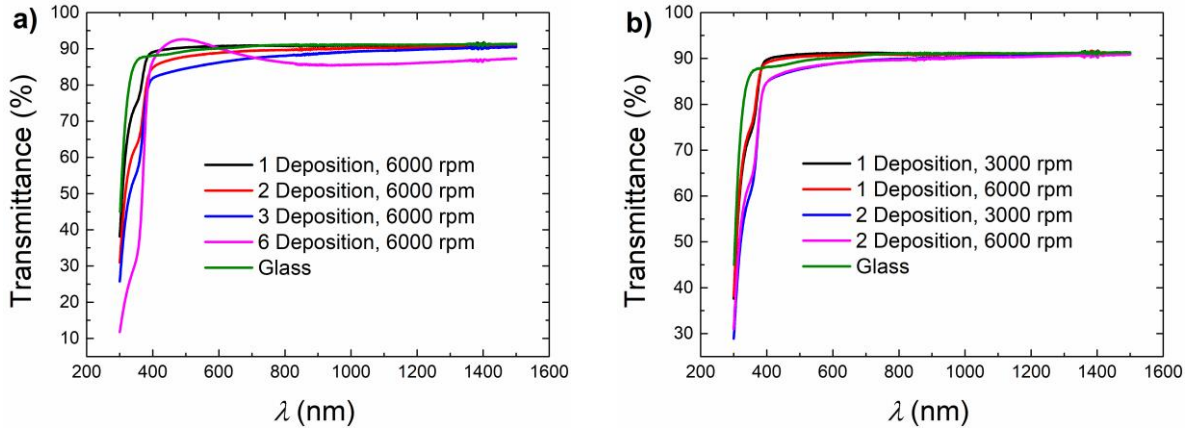

Figure 8: Influence of a) depositions number and b) spinner rotation speed on ZnO thin films transmittance spectrum. Depositions accomplished by one-step program spin coating of 3000 rpm and 6000 rpm with a final annealing step of 200 °C for 30 min.

Similar results were obtained for the ZnO thin films, except for the transmittance values. Figure 8 a) reveals a transmittance decrease with the thickness increase. As in TiO_2 case, the increase in rotation speed did not reveal any significant change to the film transmittance, as proved by Figure 8 b). However, ZnO thin films reach a constant transmittance at approximately 90 % in most of the visible spectrum, which means that they are more transmissive than TiO_2 thin films.

Concerning the CuSCN layer (HTL), the results were similar to ZnO, and high transmittances were obtained, decreasing insignificantly as the rotation is increased. In this case, it was only varied the rotation speed of the spinner and studied the influence on transmittance and reflectance curves, as is shown in Figure 9:

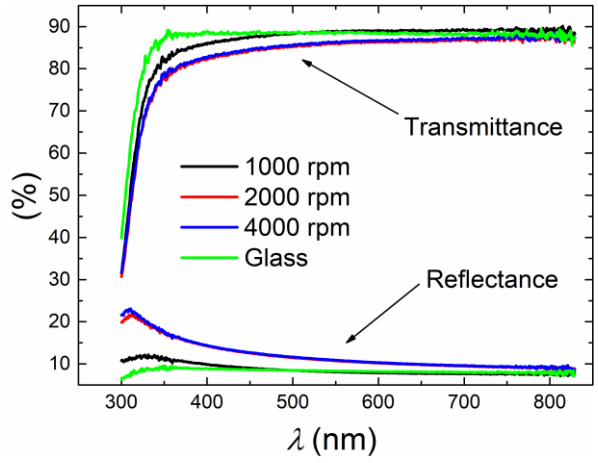

Figure 9: Influence of rotation speed on transmittance and reflectance of CuSCN layer deposited on glass. Depositions accomplished by spin coating at 1000 rpm, 2000 rpm and 4000 rpm with a final annealing step of 90 °C for 30 min.

The high transparency and low thickness of the ZnO and CuSCN layers did not allow determining their thickness by fitting the curves with the TMM analytical program, nor by profilometry. However, the XRD results of Figure 6 show, for ZnO, a thickness, at least, >20 nm, which is close to the expected value (30 nm) using the solution mentioned, as observed by Yanming Sun and co-workers. [36] Regarding CuSCN, the results show thicknesses between 80-100 nm, measured by cross section SEM images (Figure 30 from **section 3 of Results and Discussion**) which is in a good agreement with K. Zhao and co-workers observations [48].

In all cases, CuSCN, ZnO and TiO_2 thin films, the transmittance quickly decreases below 350 nm reaching values close to 0 %. In these cases, it is not possible to rigorously determine the band gap since, as the films are too thin, the absorbance spectra behavior is manly dominated by the glass. Thus, it was assumed the theoretical band gaps of 3.8, 3.3 and 3.2 eV, respectively.

Right after the optimization of these layers on top of glass, and thickness estimation, it was necessary to study the behavior when deposited on top of FTO coated glass. In this way, new transmittance, reflectance and absorbance curves were accomplished, as well as a study of their reproducibility (shown in Figure 36 from **section 4 of Appendices**).

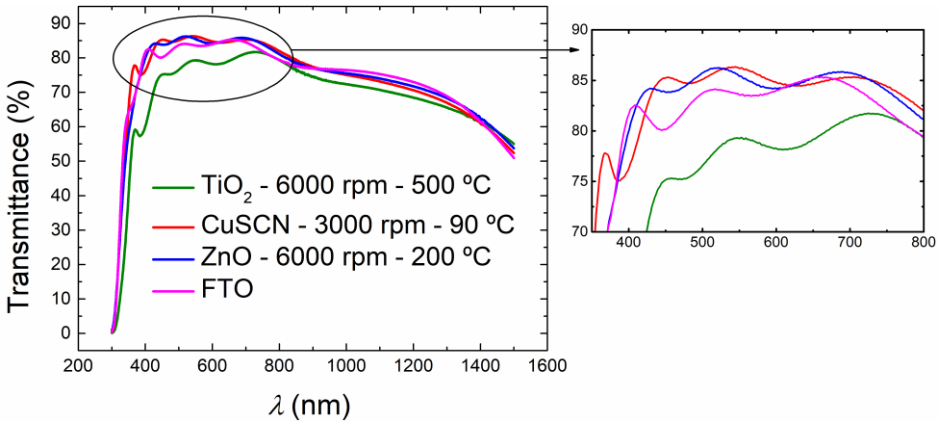

Figure 10: Transmittance curves of ETL, ZnO and TiO_2, blue and green respectively, and HTL, CusCN, red deposited with the final defined conditions for solar cells fabrication. The right inset presents a zoom where we can see the increase and decrease in transmittance, compared with FTO layer, of ETL and HTL layers.

Figure 10 represents the direct transmittance curves of ETLs and HTL over FTO coated glass, in order to study their behavior in the visible range of the light spectrum. As revealed by the curves, only TiO_2 compact layer shows a significant transmittance decrease, compared with the FTO spectrum, due to its higher refractive index relative to FTO (thus increasing reflection). In the cases of the ZnO and CuSCN spectra, it is noteworthy a small increase of transmittance which is due to the lower refractive index of these materials compared to FTO. In addition, the transmittance reaches values between 80 – 85 %, which is remarkable, since the transmittance remains high even with two distinct layers deposited on glass.

Comparing both materials for ETL, the ZnO showed higher transparency than TiO_2, which means that optically ZnO can be a better material for the purpose. However, ZnO will not be used for the electron transport layer since it was not possible to deposit a uniform perovskite film over it, as will be discussed below. Regarding the CuSCN, although it is not used over FTO, the transmittance analysis is important since it is important to achieve low parasitic absorption in the rear-located HTL.

In this way, Li^+ doped and non-doped compact and mesoporous TiO_2 transmittance was analyzed since it will also work as ETL.

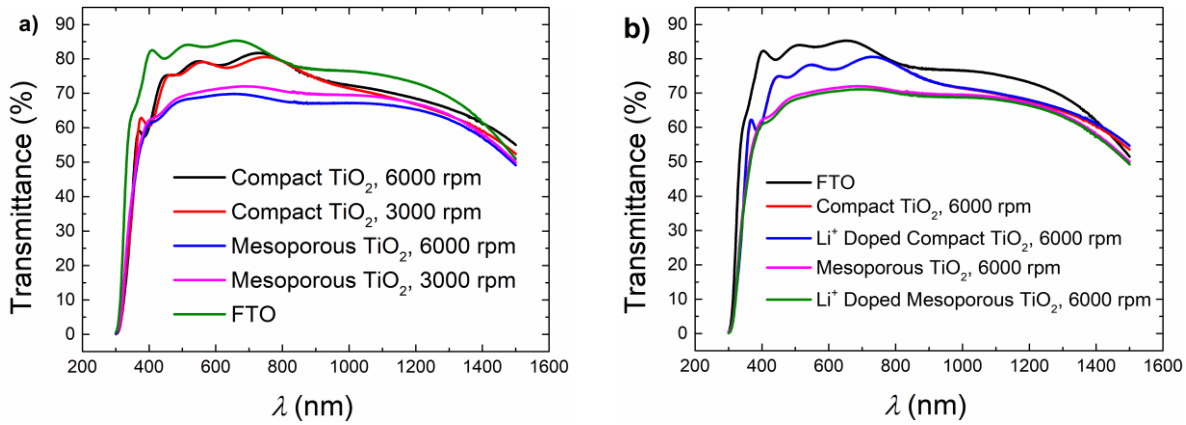

Figure 11: Transmittance spectrum of a) non-doped and b) Li^+ doped compact and mesoporous TiO_2 thin films. Depositions accomplished by one-step program spin coating of 6000 rpm, for TiO_2 deposition, and 3000 rpm, for Li^+ doping, with a final annealing step of 500 °C for 30 min. Note that in b) the red curve is barely visible since it matches the blue curve.

In both Figure 11 a) and b) the compact and mesoporous transmittance remain approximately constant with both rotation speed variation and Li^+ doping. Thus, for solar cells fabrication it was used rotations speeds of 6000 rpm, since a film homogeneity improvement was observed with such higher speed. Besides, it was observed a transmittance decrease for mesoporous TiO_2 which is due to the formation of heterogeneous thicker films (assumed to be > 100 nm, as described in literature). In addition, it was tested Li^+ doped TiO_2 in solar cells performances since Fabrizio Giordano et al. observed a TiO_2 resistivity improvement by Li^+ doping, leading to better efficiencies due to better charge collection. [47]

1.3. AFM characterization

The surface topography is an important factor of Perovskite solar cell layers since the light-surface interaction can increase the light absorbance and the surface morphology strongly influences the quality of the films wet-patterned on top. Thus, it is important to optimize the roughness levels in order to increase the light scattering, reduce light reflections to exterior and help getting compact and dense perovskite films. For that, the surface topography of ETLs were examined by AFM and surface roughness (Rms) and topographic images were analyzed in the data analysis software Gwyddion. Figure 12 shows the surface topography of FTO and TiO_2 and ZnO layers deposited over FTO:

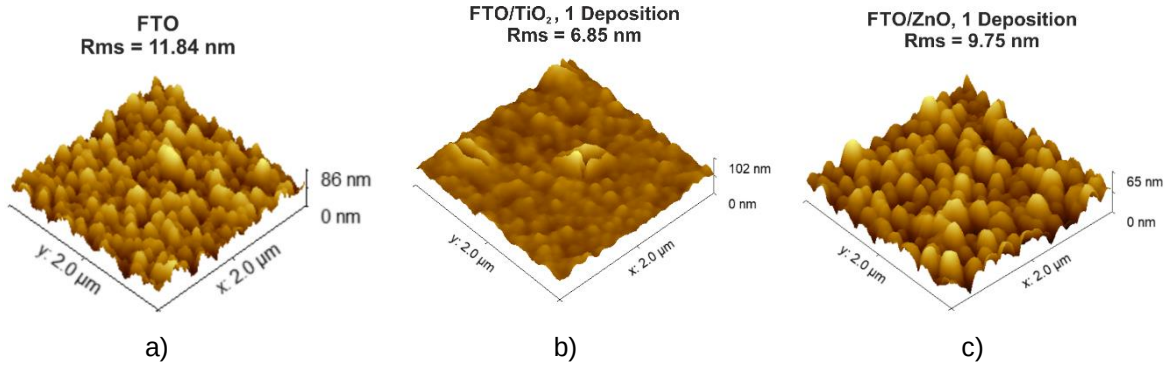

a) b) c)

Figure 12: 3D AFM images of a) FTO coated glass, b) FTO coated glass with approximately 30 nm of TiO_2 and c) FTO coated glass with approximately 30 nm of ZnO, deposited with final defined conditions. Rms determination in data analysis software Gwyddion.

From this analysis it is possible to realize that all surfaces have roughness levels between 6 - 12 nm. As expected, the roughness slowly decreases with the ETL deposition due to the filling of spaces between the FTO surface features. Therefore, the results are in a good agreement with the expectation since the FTO films exhibit the higher roughness (Rms). On the other hand, the FTO/TiO_2 film exhibits a lower roughness compared with FTO/ZnO films, which can be related with the higher film density of TiO_2.

The corresponding 2D AFM images are represented in Figure 41 from **section 8 of Appendices**, showing that all samples present a good uniformity. However, Figure 41 b) shows the presence of many defects on the FTO/TiO_2 layer, which may lead to problems in the perovskite deposition step or crystallization.

2. Perovskite Characterization

For this section it was made, initially, a state-of-the-art review of the main techniques used to improve the perovskite morphology. Then, when collected the overall conditions, it was applied and idealized a standard set of conditions. To study the influence of each individually, it was varied each condition maintaining the others the same as the standard.

The perovskite thin films deposition by spin-coating was the most challenging step of this work, since the uniformity of the obtained film changes very easily depending on the substrate and solution deposition temperature and, especially, the way we drop the non-coordination solvents

(chlorobenzene/toluene) in the second step of perovskite deposition. The following Figure 13 shows some images of both cases:

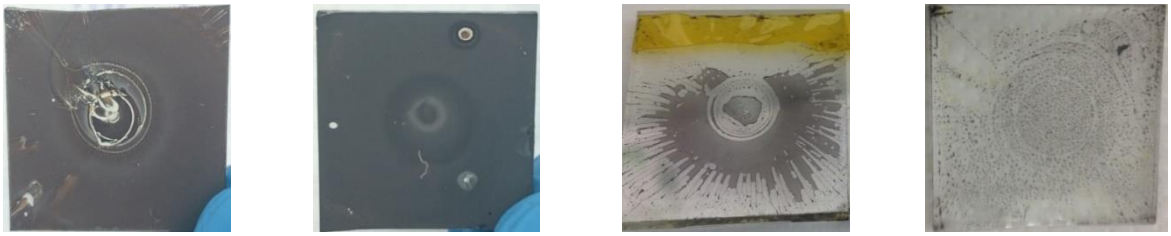

a) b) c) d)

Figure 13: Example of a) and b) bad chlorobenzene/toluene drop and c) and d)) bad TiO_2 surface coverage. The TiO_2 and $MAPbI_3$ depositions were accomplished by one-step spin coating of 6000 rpm and final annealing step of 500 °C for 30 min, and two-step spin coating (1000 rpm for 10 s and 6000 rpm for 20 s) dropping, in final seconds, 100 µL of chlorobenzene and annealing at a temperature of 100 °C for 1 h, respectively.

In one hand, a bad chlorobenzene/toluene drop may originate bad uniformities which is not desirable, as revealed by Figure 13 a) and b), since it may lead to short-circuit situations. In this way, the chlorobenzene/toluene should be dropped at once, quickly and in the sample center. On the other hand, when TiO_2 is cooled down, i.e, when it is already crystallized in anatase phase, it may be "hydrophobic" to the solution, leading to a bad perovskite solution adhesion to the substrate. Such situation is revealed by Figure 13 c) and d). However, with UV ozone and thermal treatment it showed a huge wettability improvement, since the TiO_2 surface was made hydrophilic.

By the end of the spin-coating and annealing process, the $MAPbI_3$ samples presented a dense black color, however it may vary depending on the deposition conditions. In addition, as the crystallization process occurs, it can be observed a change in the color from a translucid white color to grey-black in $MAPbI_3$ perovskites, as is possible to see in Figure 14:

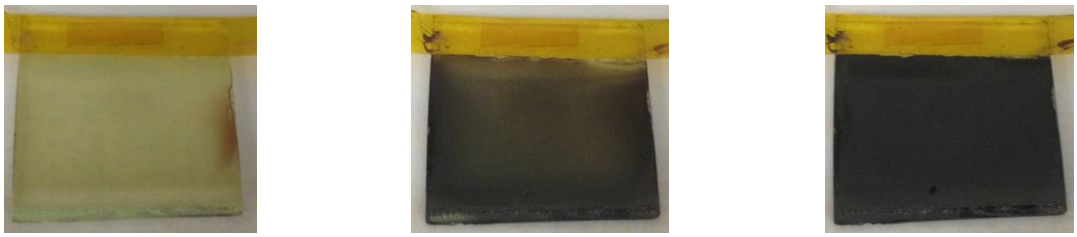

a) b) c)

Figure 14: Perovskite thin films appearance after a) placed on hot plate, b) after ≈ 3 s and c) ≈ 8 s of annealing at 100 °C.

Although all samples turn the color from translucid white to grey-black, another challenge is to achieve the desired phase, which can be cubic, tetragonal and orthorhombic, as described in introduction. In this way, some factors were changed, in the deposition step, in order to optimize this layer. It should be noted that the results presented below are the most common cases in a batch of 8 – 10 films.

2.1. Substrate and solution pre-heating temperature variation (Hot casting)

The substrate/solution pre-heating temperature was the first factor being studied since it was observed a huge improvement on perovskite films homogeneity, just by varying this temperature from 25 °C to 70 °C. In a first attempt, it was used only 1.5 M solutions, due to the higher viscosities, therefore, the films were darker and with a better uniformity. However, after this optimization, both concentrations (1 M and 1.5 M) were used for the following studies and even for solar cells fabrication. In this way, Figure 15 shows this temperature variation for perovskite precursor solution of 1.5 M:

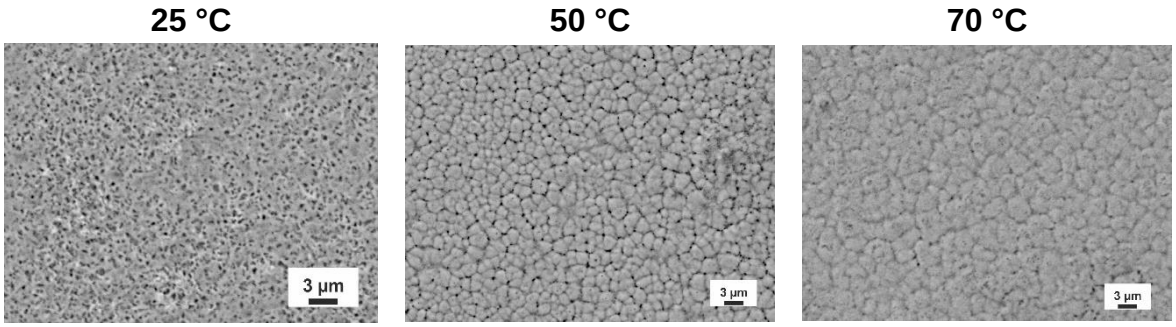

Figure 15: SEM images of perovskite thin films over compact TiO_2 deposited over FTO coated glass with 1.5 M solution and substrate temperature of a) 25 °C, b) 50 °C and c) 70 °C. The depositions were accomplished using two-step program spin coating (1000 rpm for 10 s and 6000 rpm for 20 s), 100 µL of chlorobenzene and annealing at a temperature of 100 °C for 1 h.

The results show a great improvement on film quality as the substrate and solution temperature increase, since it is perceptible no pinholes formation for temperatures higher than 25 °C. Besides that, it is remarkable the formation of close-packed grain domains for temperatures above 25 °C, which means the achievement of the right phases explained by the faster solvents evaporation and, thus, the faster reaction between perovskite solution reagents (MAI and PbI_2). Hence, the nucleation process has a smaller interaction with the environment, avoiding the degradation by humidity. In addition, at higher temperatures, the solution has a higher wettability and, shortly after propagation over the entire surface of the sample, part of DMF evaporates and $MAPbI_3$ crystals are less favorable to dissolve. In this way we achieve better conditions for grain growth.

The transition of 50 °C to 70 °C allowed the formation of larger grain domains, where is possible to measure a grain size average (ten measurements for sample) of 1.80 ± 0.55 µm and 2.92 ± 0.48 µm, respectively. These results resemble those of state-of-art perovskite solar cells and are desired, since the bigger the grain domains the lower the amount of grain boundaries and, therefore, the lower the amount of recombination. It should be noted that the distance between grains, which is observed in Figure 15 b) but not in Figure 15 c), may be simply caused by the time of exposure to the electron beam of SEM system.

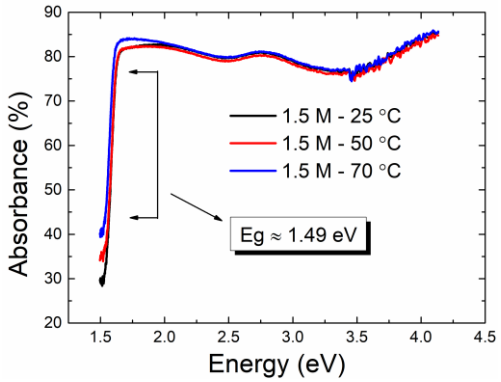

Figure 16: Influence of 1.5 M solution and substrate pre-heating temperature in absorbance spectra. The depositions were accomplished by two-step program spin coating (1000 pm for 10 s and 6000 rpm for 20 s), 100 µL of chlorobenzene and annealing at a temperature of 100 °C for 1 h. The band gap was obtained by making a linear fit in the drop zone of the curve and obtaining the intersection point with the X-Axis using the line equation (Y = mX + b).

Regarding the absorbance (Abs = 100% – T_{Total} – R_{Total}) spectra in Figure 16, the higher absorbance is reached with the higher pre-heating temperature, which is may be due to the better film uniformity and the inexistence of film vacancies. However, the absorbance variation between them is very low, reaching values of 82 - 85 %. Regardless of the absorbance variation, all samples showed an abrupt decrease at ≈ 1.5 eV. Making a linear fit in this region, is possible determine a band gap of

approximately 1.49 – 1.5 eV, which is in a good agreement with literature (e.g. of record-efficient perovskites) and which is very close to the optimum band gap.

2.2. Amount of non-coordination solvent

The amount of chlorobenzene/toluene was a factor already studied by other authors, where they found to be helpful on film coverage and morphology. In this way, the amount of this reagent was varied between 80 µL – 200 µL in order to study its influence on film morphology and grain size. Figure 17 shows SEM images which also reveal the influence on polycrystalline grain domains size:

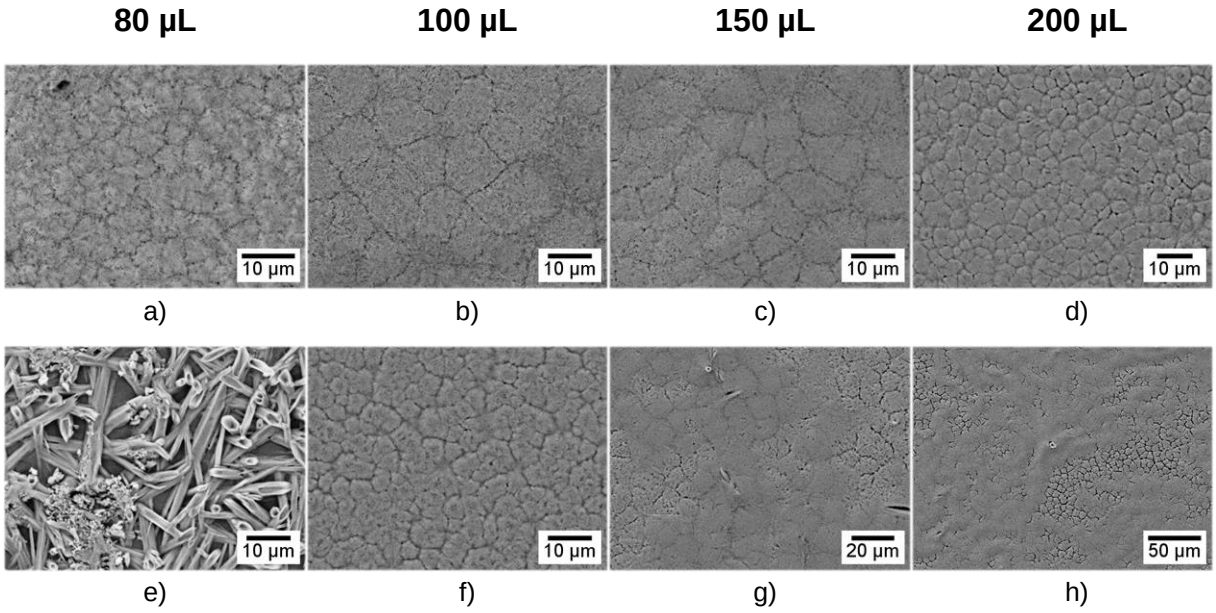

Figure 17: Influence of chlorobenzene on $MAPbI_3$ thin films morphology and grain size deposited over compact TiO_2. The films were deposited by two-step program spin coating, 1000 rpm for 10 s and 6000 rpm for 20 s, using 1 M, a), b), c), d), and 1.5 M, e), f), g), h), solutions and a final annealing at a temperature of 100 °C for 1h.

As described in the introduction, the chlorobenzene or toluene drop is a step used to increase the nucleation speed by removing the excess of DMF and DMSO (perovskite precursor solution solvents), which allows once more a smaller interaction with the environment, avoiding the degradation by humidity. Besides, is important to use the smaller DMF amount in solution as possible, during the annealing step, since $MAPbI_3$ crystals are very soluble to this solvent. Increasing the chlorobenzene amount, the evaporation rate is increased and the nucleation is faster, producing grains with an measured size between 3 and 11 µm, depending also on solution concentration. The following table resumes the grain size results of an average of ten measurements per sample using SEM imaging analysis:

Table 2: Influence of solution concentration and chlorobenzene amount on $MAPbI_3$ grain domain size, deposited over compact TiO_2. Determination based on an average of ten measurements per sample using CorelDRAW software.

Grain Size (µm)	**80 µL**	**100 µL**	**150 µL**	**200 µL**
1 M	-	9.55 ± 2.25	7.30 ± 1.93	4.73 ± 1.06
1.5 M	-	4.33 ± 0.57	10.49 ± 2.40	6.14 ± 0.79

As revealed by Figure 17 and Table 2, the bigger grains were obtained using 100 – 150 µL of chlorobenzene, being smaller or inexistent using 80 µL. Figure 17 e) depicts a typical situation of a bad crystallization, where, instead of cubes, spikes are present. This crystallization is perceptible at

naked eye, being characteristic of a light grey film, as Figure 44 a) from **section 11 of Appendices** reveals. Besides, when no chlorobenzene is added during the spin coating process, it was observed a poor surface coverage in most cases, hence it was not studied to avoid wastes. This coverage improved with the chlorobenzene volume added, with films becoming smoother and appearing more continuous with the increase of chlorobenzene.

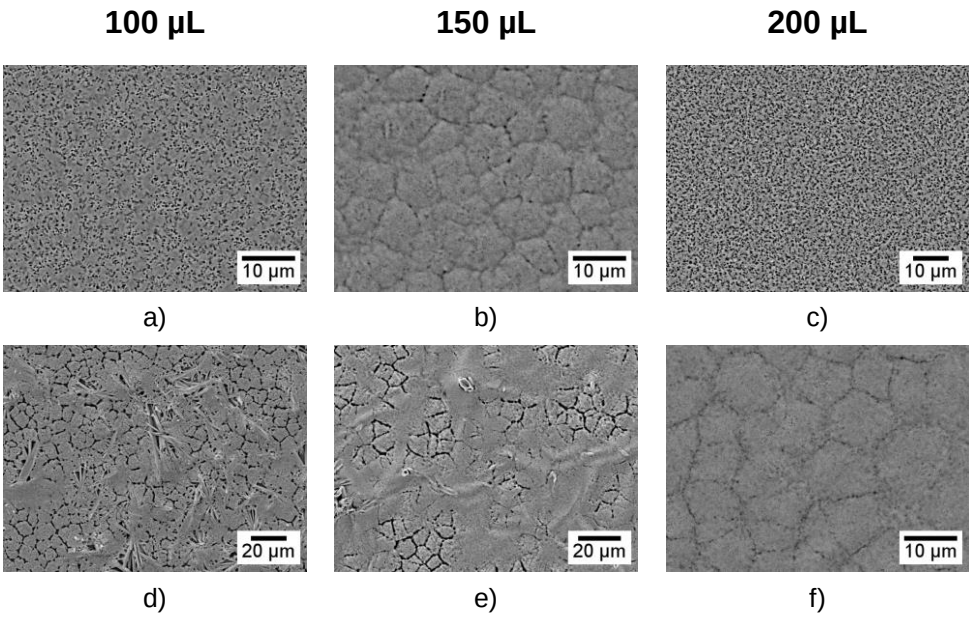

Figure 18: Influence of Toluene on $MAPbI_3$ thin films morphology and grain size deposited over compact TiO_2. The films were deposited by two-step program spin coating, 1000 rpm for 10 s and 6000 rpm for 20 s, using 1 M, a), b), c), and 1.5 M, e), f), g), solutions and a final annealing at a temperature of 100 °C for 1h.

Table 3: Influence of solution concentration and Toluene amount on $MAPbI_3$ grain domain size deposited over compact TiO_2. Determination based on an average of ten measurements per sample using CorelDRAW software.

Grain Size (µm)	**100 µL**	**150 µL**	**200 µL**
1M	-	7.97 ± 1.51	-
1.5 M	8.09 ± 1.61	7.86 ± 1.35	9.19 ± 1.37

In the toluene case, the results were similar, Figure 18, differing in the films color. Here the films presented a darker black color, and the grain size increased with the content of toluene. However, the higher reproducibility, larger grain size, more uniform and consistent films were obtained using chlorobenzene.

2.3. Solvents (DMF:DMSO) ratio variation

The DMF:DMSO solvent ratio is known to be an important factor on perovskite films fabrication. As explained by Bing Cai et al., DMSO has a low evaporation rate and high viscosity working both as a solvent and as a coordination reagent, in the form of PbI_2-MAI-DMSO complex, while DMF only functions as a solvent with higher evaporation rate. In addition, the best performance was achieved with 4:1, 3:2 and 2:3 DMF:DMSO ratios [27]. In this way, the mix between the reagents has the purpose of combining both properties in order to achieve the best film uniformity.

Here it was tested only with 4:1 and 1:4 ratios and studied their influence on precursor solutions and perovskite films, as is shown in Figure 19:

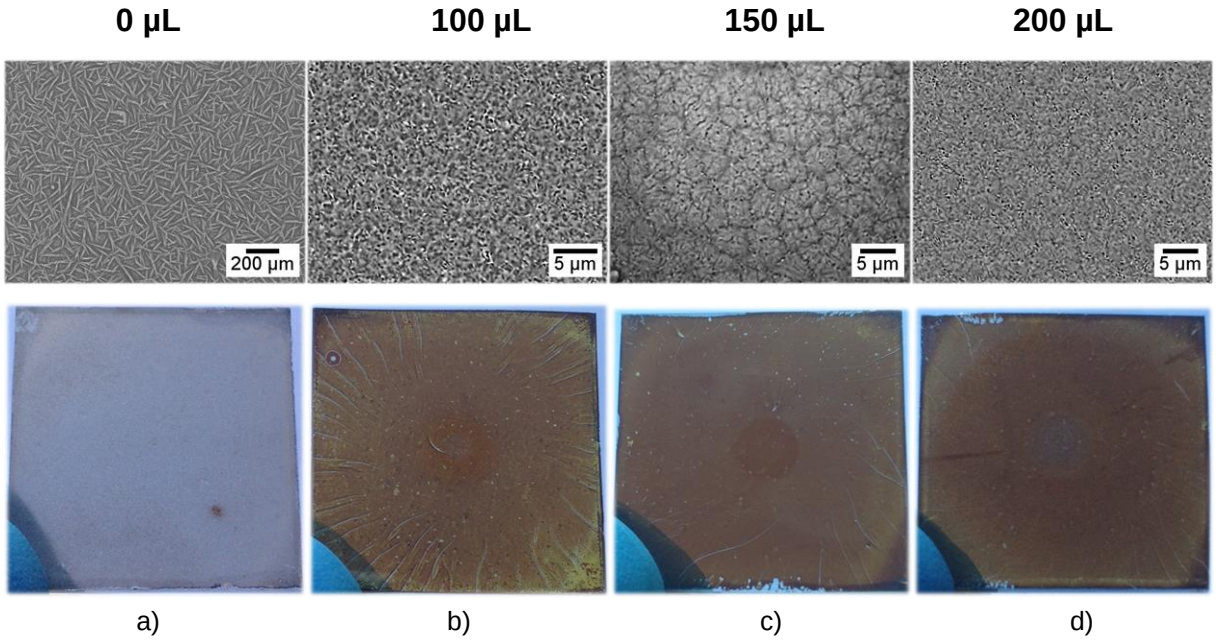

Figure 19: Influence of 1:4 DMF:DMSO ratio on $MAPbI_3$ thin films morphology and grain size, deposited over compact TiO_2. Films were deposited with solutions and substrates at 70 °C by two-step program spin coating, 1000 rpm for 10 s and 6000 rpm for 20 s, dropping different chlorobenzene amounts in the final seconds, using 1 M solution. The annealing step was accomplished for 1 h at 100 °C.

For 1:4 DMF:DMSO ratio, the first observation was the precursor solution reagents solubility. In this case, the 1 M solutions had a great difficulty to solubilize the reagents even when left on the hot plate at 70 °C. On the other hand, it was not possible the fabrication of 1.5 M solutions due to the poor solubility, demonstrating that DMF is a critical solvent to control the precursor solutions concentration. Regarding the film homogeneity, with this ratio a good homogeneity is not possible and the final color becomes a transparent brown instead of the desired dark grey/black film. Therefore, the absorbance curves show a fast decrease, as is expected and revealed by Figure 20:

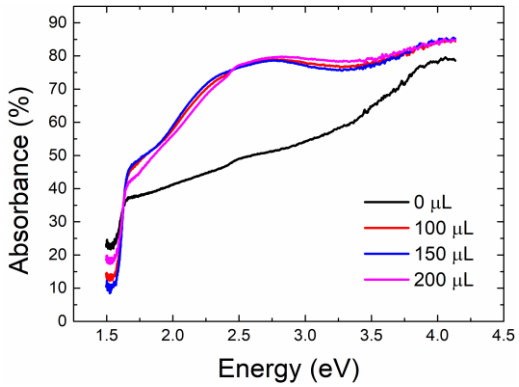

Figure 20: Influence of 1:4 DMF:DMSO ratio with different chlorobenzene amounts in the absorbance spectra. Depositions accomplished by two-step program spin coating (1000 pm for 10 s and 6000 rpm for 20 s) dropping different amounts of chlorobenzene in final seconds with annealing at a temperature of 100 °C for 1 h. The band gap was obtained by making a linear fit in the drop zone of the curve and obtaining the intersection point with the X-Axis using the line equation (Y = mX + b).

Besides all observations, the presence of perovskite is proved by the abrupt decrease at approximately 1.5 eV in the absorbance spectra, which is due to the perovskite band gap.

For 4:1 DMF:DMSO ratio, no difficulty in solubility was observed, being the solubilization possible at room temperature. Here the solvent mix properties are controlled by DMF, being the solution less viscous, and the DMSO works mainly as the coordination reagent. The formation of the PbI_2-MAI-DMSO intermediate-phase film retards the rapid reaction between PbI_2 and MAI during the

evaporation of DMF. However, after the DMF evaporation, a fast crystallization is essential for less degradation by humidity. Thus, this intermediate phase helps not only the grain formation as in the film homogeneity, as described in introduction and as possible to see in, for example, Figure 44 b) of **section 11 of Appendices**.

2.4. Substrate coating variation

Until this section, all parameters were varied and tested producing perovskite films over compact or mesoporous TiO_2, since the main objective is to produce a complete solar cell structure. However, the film's morphology, homogeneity and grain size may be affected by the surface where it will be deposited and crystallize. In this way, perovskite thin films were produced in glass substrate coated with different materials, and analyzed by SEM.

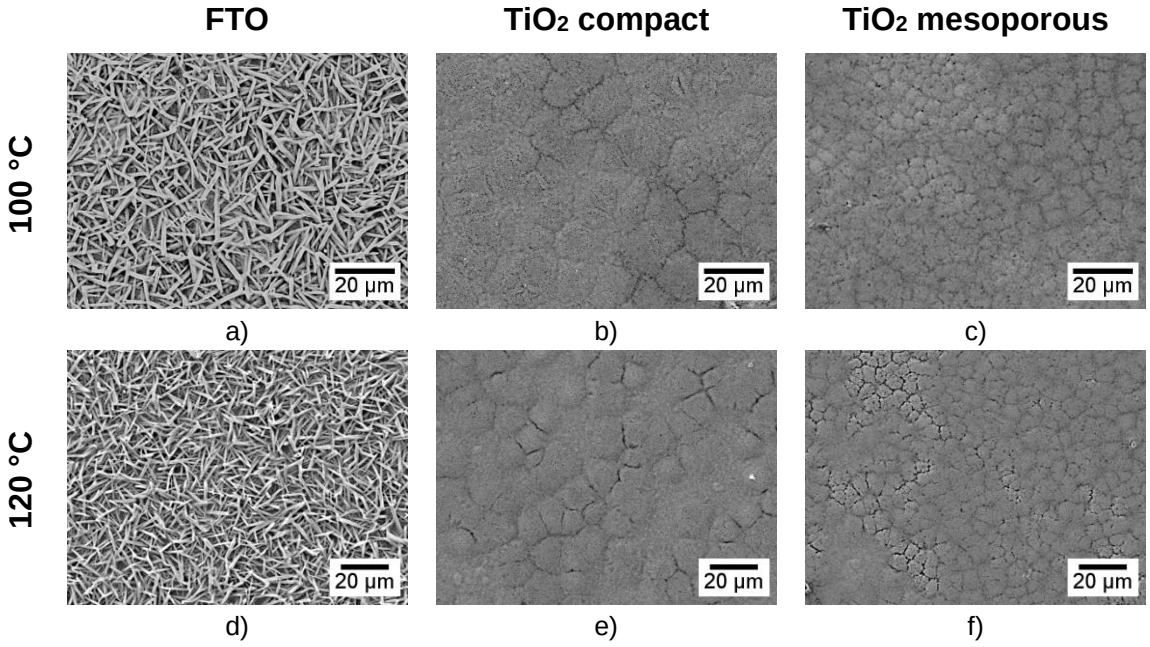

Figure 21: Influence of substrate on $MAPbI_3$ thin films morphology and grain size, deposited with solutions and substrates at 70 °C by two-step program spin coating, 1000 rpm for 10 s and 6000 rpm for 20 s, dropping 150 µL of chlorobenzene in final seconds, using 1.5 M solution. The annealing step was accomplished for 1 h at 100 °C and 120 °C.

The first observation of this study was the hydrophilic behavior of each substrate, since it is an important factor on the film homogeneity. For FTO and mesoporous TiO_2, the solution spread all over the substrate with no need of UV or temperature treatment, and using approximately 90 µL of perovskite precursor solution. In the compact TiO_2 case, as discussed previously, at room temperature the surface may be hydrophobic to the perovskite solution, thus requiring UV treatment.

Regardless of annealing temperature, the SEM images reveal, for FTO substrates (Figure 21 a) and d)), a $MAPbI_3$ crystallization in the form of spikes which is clearly not the desired morphology. On the other hand, the desired film morphology was achieved using a compact or mesoporous TiO_2 layer, Figure 21 b), c), e) and f), where the higher polycrystalline grain size was obtained using a compact layer with an average of 12.34 ± 2.72 µm and 10.77 ± 2.19 µm for 100 °C and 120 °C, respectively, compared to 5.16 ± 1.3 µm and 5.76 ± 0.89 µm when deposited over mesoporous TiO_2 layer at 100 and 120 °C, respectively.

As is expected, varying the substrate coating for the perovskite deposition leads to absorbance variations, since it influences the perovskite material and respective thickness.

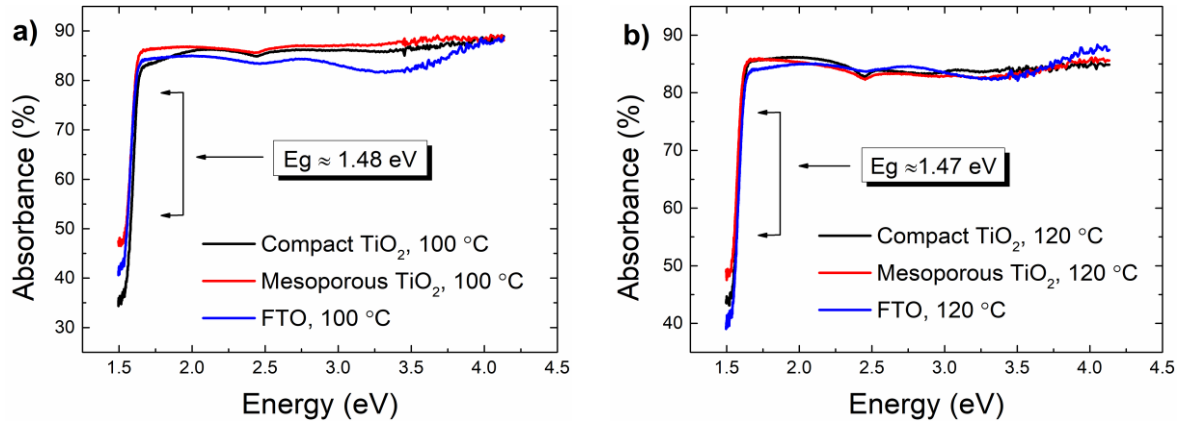

Figure 22: Influence of different substrate coatings on the absorbance spectra of the deposited perovskite films. The depositions were accomplished by two-step program spin coating (1000 pm for 10 s and 6000 rpm for 20 s), dropping 100 µL of chlorobenzene in final seconds, and annealing at a temperature of a) 100 °C and b) 120 °C for 1 h, using 1.5 M solutions. The band gap was obtained by making a linear fit in the drop zone of the curve and obtaining the intersection point with the X-Axis using the line equation (Y = mX + b).

In this study, the higher absorbance was obtained for annealing temperatures of 100 °C. In addition, a greater variation of the absorbance with the variation of the substrate coating was expected, which may be observed at least for higher wavelengths. However, this study reveals an insignificant perovskite absorbance variation with different substrate surfaces. Besides, all samples reach absorbances close to 85 - 87 % and show a band gap of 1.48 eV and 1.47 eV to 100 °C and 120 °C, respectively.

For ZnO (ETL) thin films, the perovskite deposition was not easy since the surface does not have the ideal wettability. Thus, as in compact TiO_2 case, a UV and temperature treatment before the perovskite deposition was required. Many attempts have been made and the best results are summarized in the following Figure 23:

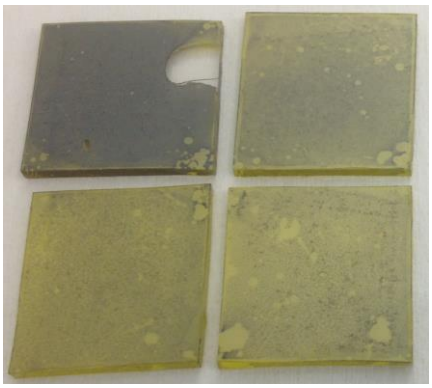

Figure 23: $MAPbI_3$ thin films morphology deposited over ZnO with solutions and substrates at 70 °C by two-step program spin coating, 1000 rpm for 10 s and 6000 rpm for 20 s, dropping 150 µL of chlorobenzene in final seconds, using 1.5 M solution. The annealing step accomplished for 1 h at 100 °C (left samples) and 120 °C (right samples).

Right after the spin coting the samples were annealed at 100 °C and 120 °C in a hot plate. Unlike TiO_2, the perovskite thin films never reached full crystallization, never becoming a dark black film, and after less than ten minutes the samples begin to change the color to yellow due to the organic component degradation. This degradation may be due to the reaction of perovskite with some remaining precursor solution reagent, since both ethanolamine and 2-methoxiethanol have a boiling point, 170 °C and 124 °C respectively, close to the compact ZnO annealing temperature (200 °C). In view of these difficulties, ZnO ETL was not used for the solar cells fabrication, and only a compact or mesoporous TiO_2 layer were applied as ETL.

2.5. Annealing temperature variation

The annealing temperature is one of the main factors in the perovskite film development. This factor has a bigger impact in the film morphology, crystallization rate and structure and in the grain domains size. As already observed by Amalie Dualeh et al., [24] for annealing temperatures below 70 °C the crystallization is not completed, independently of the time. For temperatures above 200 °C the crystallization was observed to occur almost instantaneously, quickly leading to a yellow coloration. Figure 24 shows SEM images of samples with different annealing temperature treatment:

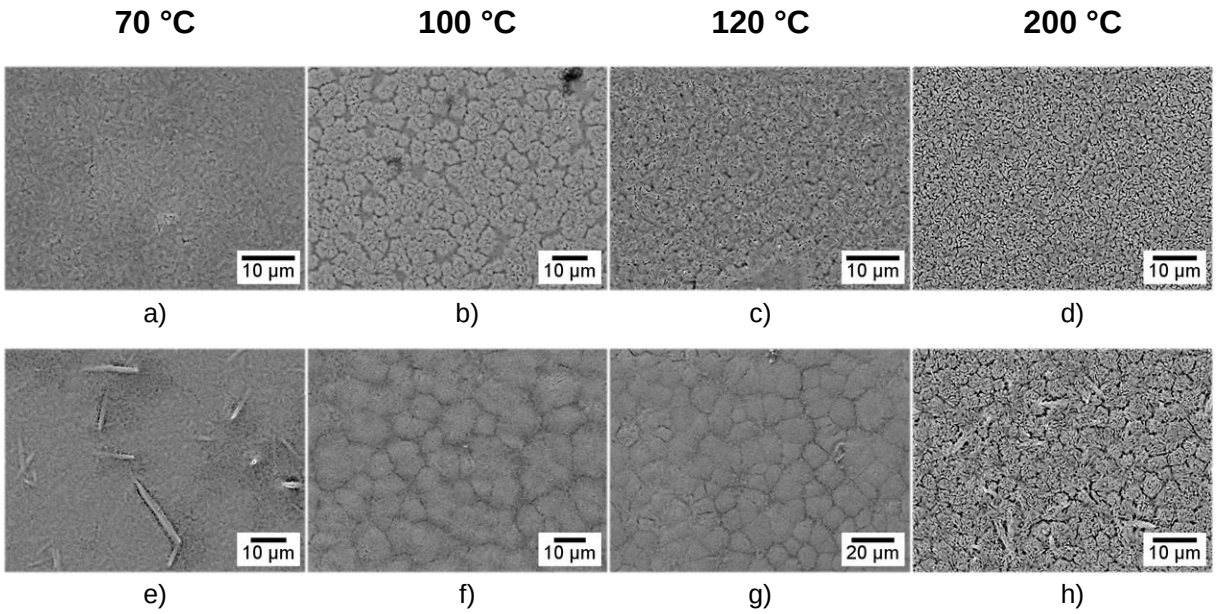

Figure 24: Influence of annealing temperature on $MAPbI_3$ thin films morphology and grain size, deposited over compact TiO_2. Films deposited with solutions and substrates at 70 °C by two-step program spin coating, 1000 rpm for 10 s and 6000 rpm for 20 s, dropping 150 µL of chlorobenzene in final seconds, using 1 M, a), b), c), d), and 1.5 M, e), f), g), h), solutions. Annealing step were accomplished for 1 h for each temperature.

The results showed a faster crystallization as the temperature increases. For 70 °C the color change only begins 2 - 3 min after standing on a hot plate, showing, after concluding the annealing step, a black transparent color and a highly homogeneous film. For both solution concentrations, 1 M and 1.5 M, the SEM results were similar showing nice coverage but inexistence or too small grains. In addition, for 1.5 M it is possible to observe the existence of spikes which may be due to the bigger concentration, i.e, for this concentration 70 °C annealing may not be sufficient to crystallize all film thickness.

Regarding temperatures higher than 70 °C, the color change appears to be instantaneous, increasing as the temperature increases. All samples showed very good coverage and as is possible to see in Figure 24 that grains start to form at 100 °C, showing bigger sizes with solutions of 1.5 M, as confirmed by Table 4:

Table 4: Influence of solution concentration and annealing temperature on $MAPbI_3$ polycrystalline grain domain size, deposited over compact TiO_2. Size determination based on an average of ten measurements per sample using CorelDRAW software.

Grain Size (µm)	**70 °C**	**100 °C**	**120 °C**	**200 °C**
1 M	-	4.86 ± 0.85	-	-
1.5 M	-	8.21 ± 2.21	9.36 ± 1.87	-

At 120 °C, on one hand, for 1.5 M the grain size appears to increase, but, on the other hand, for 1 M, Figure 24 c) reveals the beginning of organic degradation, showing film vacancies and grains not well defined. This reveals that 120 °C may be too high for films produced with 1 M solutions. Thus, the best annealing temperature changes with the solution concentration, being 100 °C ideal for 1 M solutions and 120 °C ideal for 1.5 M solutions. However, XRD results, Figure 42 from **section 9 of Appendices**, show a more intense PbI_2 peak for annealing temperatures of 100 °C, and less intense for 120 °C, which reveals a better crystallization for the higher annealing temperature.

With $MAPbI_3$ thin films deposited over mesoporous TiO_2 layer (Figure 38 from **section 5 of Appendices**), we only studied annealing temperatures of 100 °C and 120 °C. In this case, the homogeneity appears to be better than depositions over compact TiO_2, which is expected due to the better wettability. No crystallization difficulties occurred, except for the annealing temperature of 100 °C using 1.5 M which give the idea of an incomplete crystallization. Despite that, SEM images show an average grain size between 3 and 6 µm (Table 11), which is lower than films deposited over compact TiO_2.

For samples heated at 200 °C, the color change to black was instantaneous but another color change occurs after two minutes, to yellow, showing the organic (MAI) component degradation. The perovskite characteristics are almost no longer distinguishable, and the absorption spectra resembles that of pure PbI_2 with slightly higher band gap of 2.27 eV, obtained by fitting curves on the drop zone. This confirms that the yellow color, Figure 45 from **section 11 of Appendices**, of these films is due to the formation of PbI_2 at these high temperatures, confirmed also by XRD results.

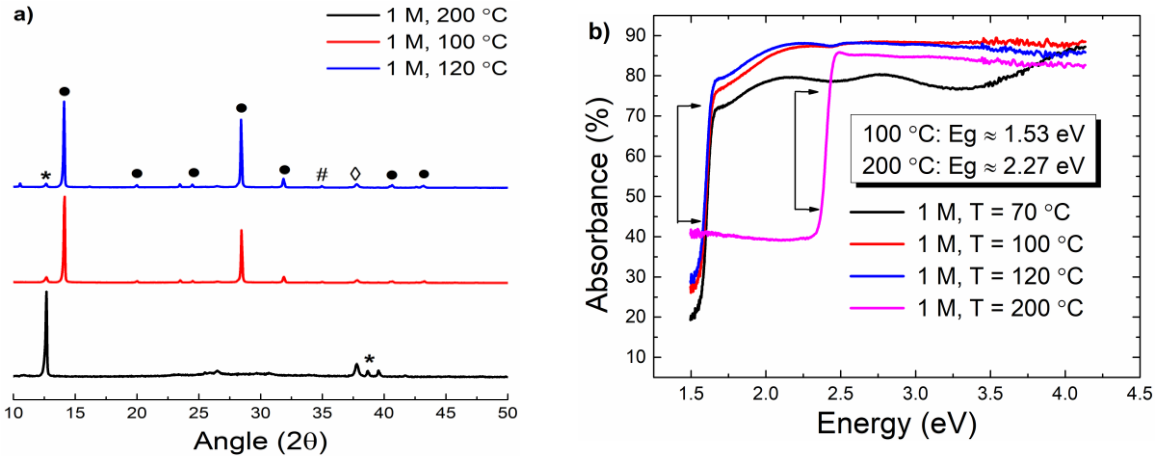

Figure 25: a) XRD and b) absorbance analysis of $MAPbI_3$ thin films, deposited over compact TiO_2, annealed at distinct temperatures. In XRD spectra, the tetragonal perovskite phase is identified by a full circle, the PbI_2 phase is identified by an asterisk and finally the CuSCN and FTO phases are identified with a cardinal and rhomb respectively. The band gap was obtained by making a linear fit in the drop zone of the curve and obtaining the intersection point with the X-Axis using the line equation (Y = mX + b).

Figure 25 a) shows the XRD comparison with different annealing temperatures for films produced with 1 M solution. The results reveal, for 100 °C and 120 °C, the presence of (110), (112), (202), (220), (310), (224) and (314) planes at an angle 2θ of 14.10°, 19.92°, 24.5°, 28.50°,31.87°, 40.55° and 43.06° which is indicative of the presence of $MAPbI_3$ tetragonal phase (marked with a full circle). [24], [27], [55], [56] On the other hand, as is expected, the peaks corresponding to the PbI_2 phase, at 12.67° and 38.7° (marked with an asterisk, [57]), are more intense for the sample annealed at 200 °C. In addition, at such higher temperature there are no perovskite phase peaks, proving the organic degradation and the formation of a PbI_2 film. The peaks corresponding to cardinal and rhomb at 34.97° and 37.77° are related to $^{\#}$CuSCN and $^{\lozenge}$FTO layers, respectively. [43], [56] Very similar XRD patterns were obtained using 1 M and 1.5 M solutions, showing for both the prevalence of $MAPbI_3$ tetragonal phase (Figure 38 from **section 9 of Appendices**).

Regarding the influence on the absorbance spectra, Figure 25 b) and Figure 37 f) of **section 4 of Appendices** show a maximum absorbance achieved at temperatures of 100 °C and 120 °C,

reaching close to 90 % for both concentrations. Besides, for 70 °C the absorbance is lower, as expected since it presented a transparent black color. However, regardless of the maximum absorbance, all samples which present perovskite film features exhibit a band gap of ≈ 1.5 eV.

2.6.

2.6. Final observations

The rotation speed of the spinner is also a factor which influences not only the perovskite thickness but also the morphology. For the perovskite deposition, a two-step spin coating of 1000 rpm for 10 s and 6000 rpm for 20 s with a 2000 rpm.s^{-1} ramp was used, where the first step is for the solution to spread all over the substrate and the second is for solvents evaporation. However, higher rotations speeds were tested in order to study their influence on uniformity and morphology, as shown in Figure 26.

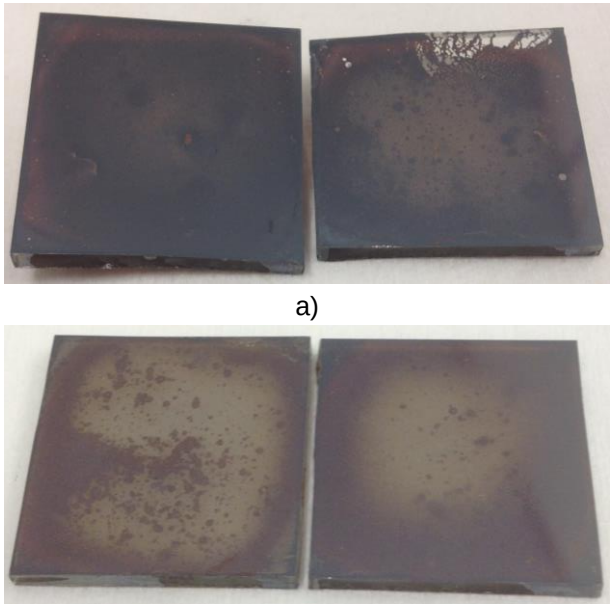

a)

b)

Figure 26: $MAPbI_3$ thin film morphologies using one-step spin coating of 3000 rpm (a) and 6000 rpm (b) with a 2000 rpm.s^{-1} ramp.

For both cases, 3000 rpm and 6000 rpm with a 2000 rpm.s^{-1} ramp, the perovskite films showed a huge degradation and very low uniformities. For that reason, the rotation speed of the spinner was maintained throughout this work even for solar cells fabrication.

3. Solar Cells Characterization

The solar cell performances are highly influenced by the perovskite films morphology and crystalline structure, i.e., by the perovskite film thickness, film uniformity, grain size, grain orientation, etc., which are highly influenced by all previous studied conditions. Besides, the ETL and HTL choice is also an important factor due to the band alignment. Thus, previous studies about ETL, HTL and perovskite layers enabled the choice of favorable conditions for the solar cells fabrication.

In this section, optical and morphological characterizations were performed after IV performances measurements, since it is convenient to measure the IVs with the shortest possible time after the solar cell fabrication. The first characterized batch was already studied in section 2.5 of this chapter, where it was varied the substrate coating and the annealing temperature, as presented in Figure 27:

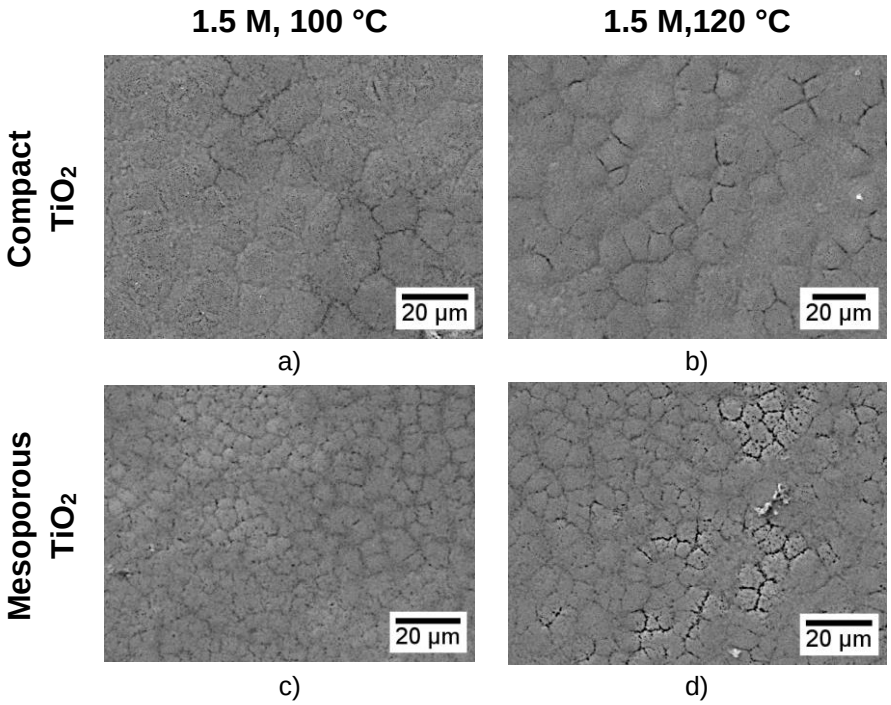

Figure 27: $MAPbI_3$ thin films morphology and grain size, deposited over compact and mesoporous TiO_2. Films deposited with solutions and substrates at 70 °C by two-step program spin coating, 1000 rpm for 10 s and 6000 rpm for 20 s, dropping 150 µL of chlorobenzene in final seconds, using 1.5 M solutions concentrations. The annealing step were accomplished at 100 °C and 120 °C for 1 h for each temperature.

In this case, it was fabricated solar cells based on 1.5 M perovskite solution concentration and annealed at 100 °C and 120 °C. The best coverage and the bigger polycrystalline grains were obtained for compact TiO_2, with an average of 12.34 ± 2.72 µm and 10.77 ± 2.19 µm, respectively, and overall optical absorbances close to 90 % already discussed in section 2.4. The EDS analysis was accomplished in order to verify the presence of all the expected materials of the complete solar cells layer structure.

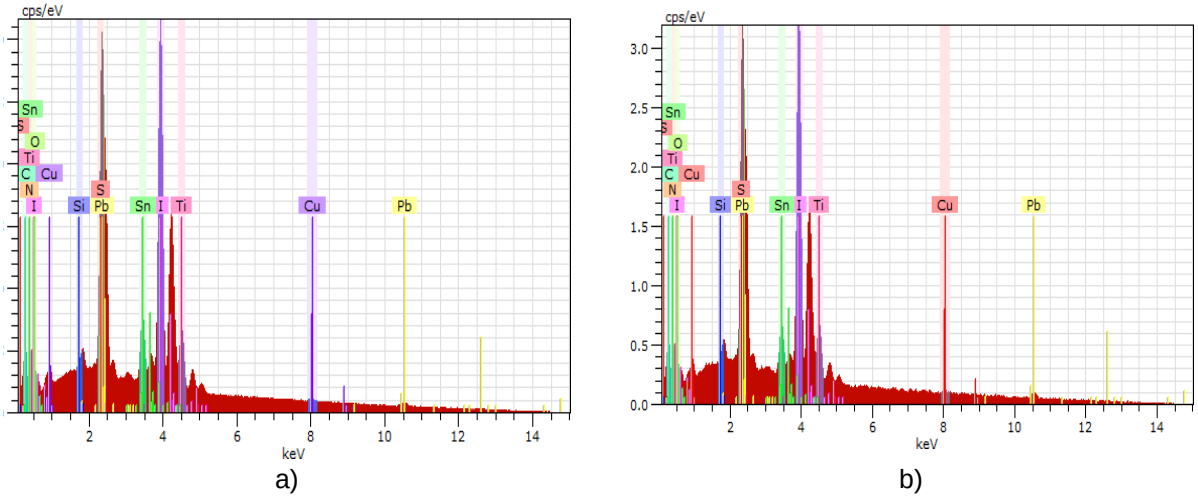

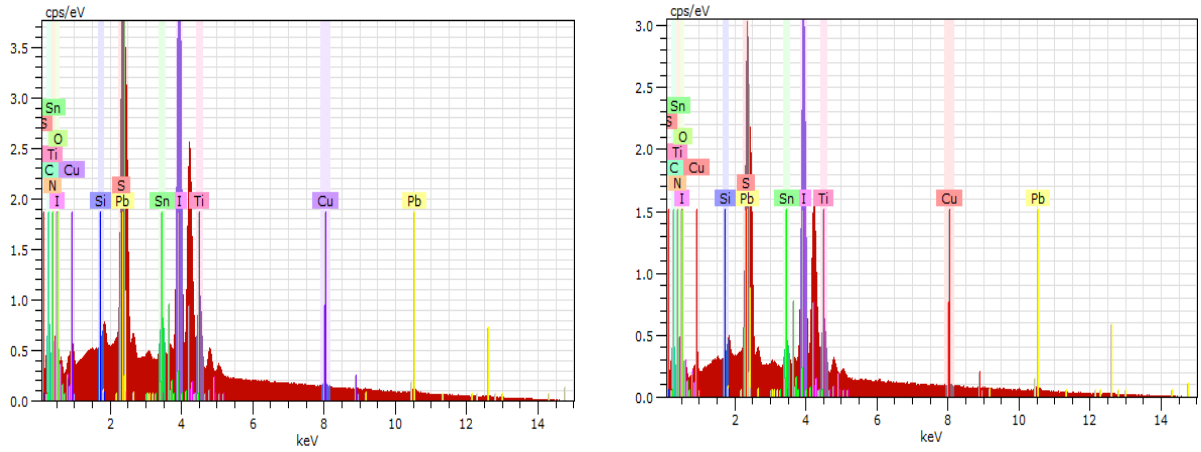

Figure 28: EDS analysis of the same $MAPbI_3$ thin films of Fig. 27, deposited over a) and b) compact (top) and c) and d) mesoporous (bottom) TiO_2 (ETL), having the CuSCN HTL on top.

Figure 28 a), b) c) and d) show the EDS analysis of the previous samples of Fig. 27, where is revealed the presence of all elements of each layer: the presence of Ti from the ETL, C, I, N and Pb from the perovskite layer ($MAPbI_3$), and finally, the presence of C, Cu, N and S from the HTL.

In this first attempt only two solar cells built over compact TiO_2 showed PV response:

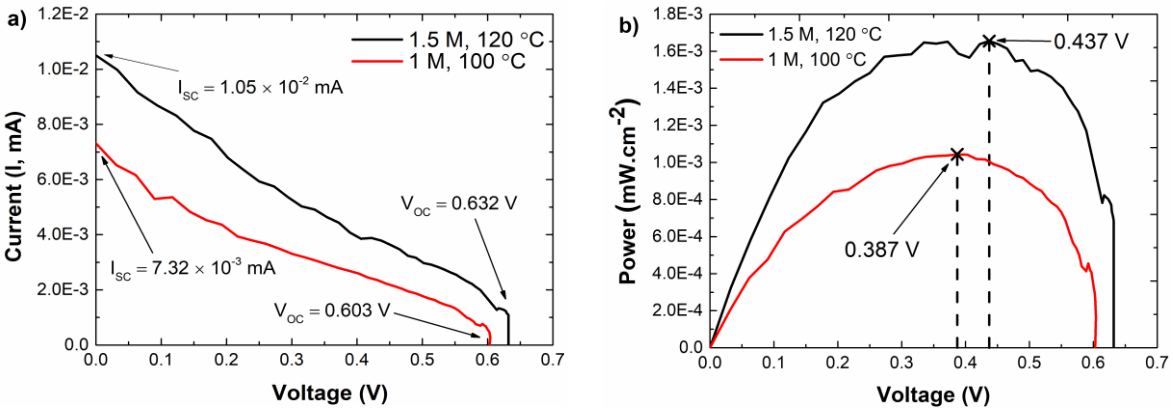

Figure 29: First solar cells: a) Current-voltage (IV) and b) Power-voltage (PV) curves performances for $MAPbI_3$ thin films deposited over compact TiO_2 using 1.5 M solutions. TiO_2, $MAPbI_3$ and CuSCN depositions were accomplished by, one-step spin coating of 6000 rpm with final annealing step of 500 °C for 30 min, two-step spin coating (1000 pm for 10 s and 6000 rpm for 20 s) dropping, in final seconds, 150 µL of chlorobenzene and annealing temperature of 100 °C and 120 °C for 1 h and, one-step spin coating of 3000 rpm with final annealing step of 90 °C for 30 min, respectively.

Table 5: IV performance results of first attempt.

Solar cells Parameters	V_{OC} (V)	J_{SC} (mA/cm^2)	FF	R_P (kΩ)	R_S (kΩ)	PCE (%)
1.5 M 100 °C	0.603	9.15×10^{-2}	0.236	83.33	14.49	0.013
1.5 M 120 °C	0.632	0.131	0.249	58.82	7.75	0.021

In this preliminary attempt, despite the relatively high V_{OC}, the IV performance shows very low current densities. From literature, it was expected better results of ≥ 1 V and tens of mA/cm^2 for V_{OC} and J_{SC}, respectively. The V_{OC} is physically limited by the perovskite band gap (≈ 1.5 eV). For J_{SC} the

results may be due to bad $MAPbI_3$ bulk coverages, as is possible to see in the following cross-section SEM images:

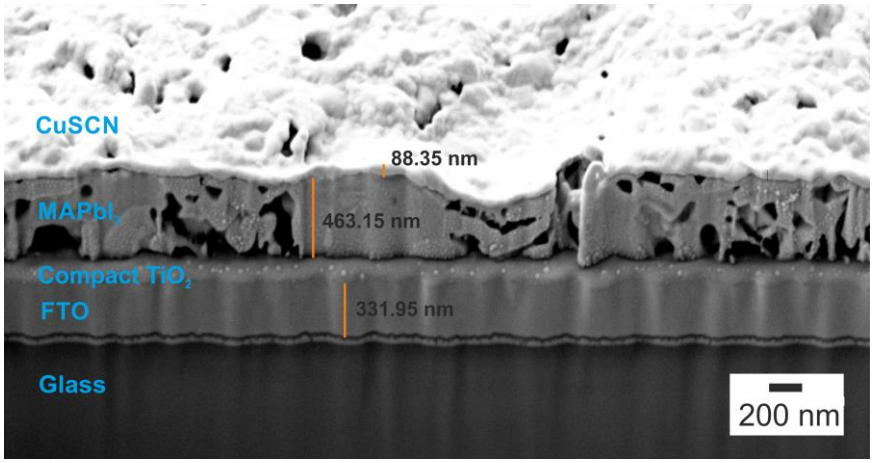

a)

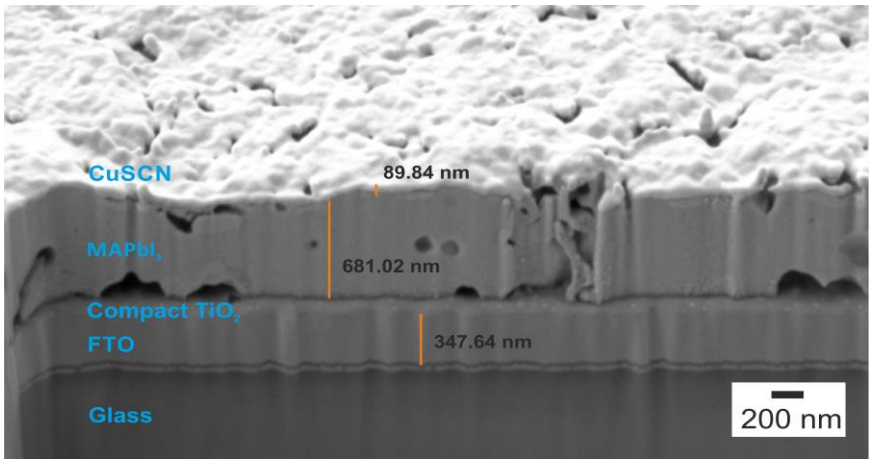

b)

Figure 30: Cross Section SEM analysis of full solar cells structure using a) 1 M and b) 1.5 M precursor solution concentration deposited over compact TiO_2.

As Giles E. Eperon et al. clarified, in one hand, if there are regions of no perovskite coverage, light will pass without absorption, decreasing the available photocurrent, and, on the other hand, insufficient coverage may result in a high frequency of "shunt paths" allowing contact between ETL and HTL. [9] Besides this ETL/HTL contact, the insufficient coverage may increase also charge trapping inducing a high recombination probability, leading to more losses.

For FF and PCE calculation it was used equation 1, 2 and 3 from Appendices, using the observed maximum voltage (from PV curves, Figure 29 b)) and respective maximum current. In this way, as is revealed in Table 5, a FF of 0.236 and 0.249 and a PCE of 0.013 % and 0.021 % were obtained for solar cells produced with 1.5 M solution concentration with final annealing step of 100 °C and 120 °C, respectively.

For both cases, the PCE results were very low, as is expected since the solar cells produced very low current densities. Besides, the low FF obtained is affected by shunt (R_P) and series (R_S) resistances behavior, which showed to be in kΩ range for both cases. For a normal solar cells performance, is needed a R_P as high as possible and a R_S as low as possible. This high Rs resistance and low Rp resistance are obtained mostly due to the low bulk uniformities, justifying the low obtained currents and, hence, the low PCEs.

In the following attempts, it was used also a Li^+ doped compact and mesoporous TiO_2 as ETL and the morphological characterization results are summarized in Figure 31:

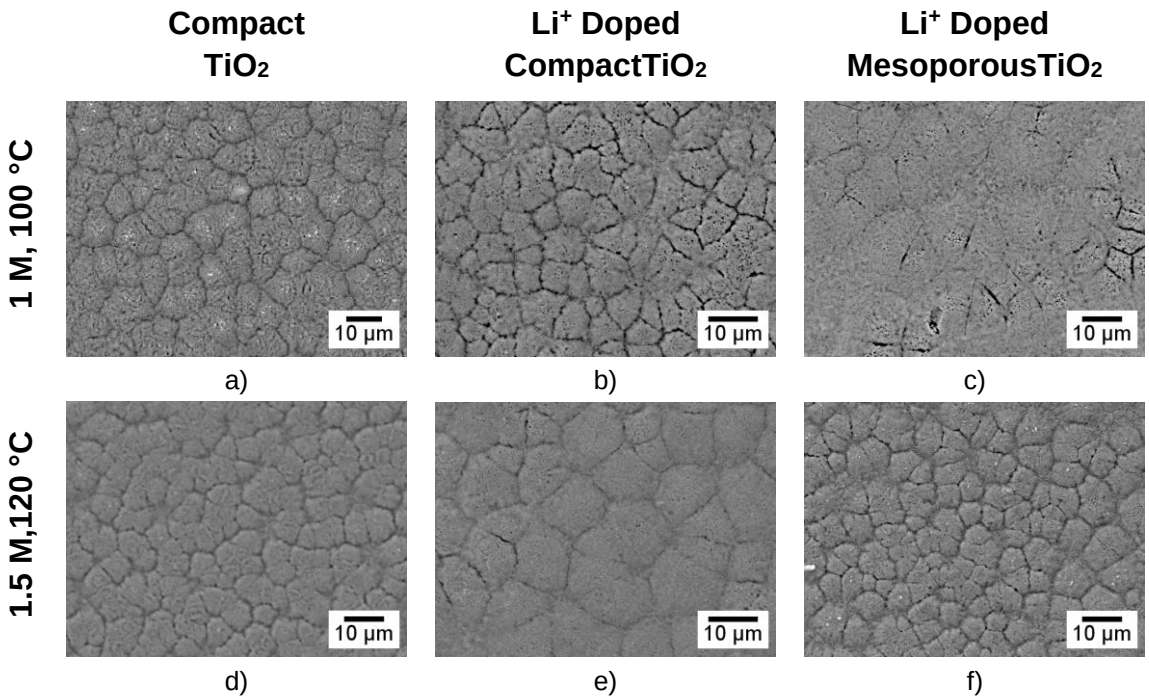

Figure 31: $MAPbI_3$ thin films morphology and grain size, deposited over Li^+ doped and non-doped compact and Li^+ doped mesoporous TiO_2. Films deposited with solutions and substrates at 70 °C by two-step program spin coating, 1000 rpm for 10 s and 6000 rpm for 20 s, dropping 150 µL of chlorobenzene in final seconds, using 1 M, a), b) and c), and 1.5 M, d), e) and f), solutions. The annealing step were accomplished at 100 °C and 120 °C for 1 h for each temperature.

The desired morphology was obtained in all samples, showing very defined polycrystalline grain domains, with an average size summarized in Table 12 from Appendices. Despite the Li^+ doping, it is not possible the detection of this element by EDS analysis, as seen in Figure 40 from **section 7 of Appendices**. In addition, the best performing devices were obtained for solar cells built over non-doped compact TiO_2, as is shown in Figure 32.

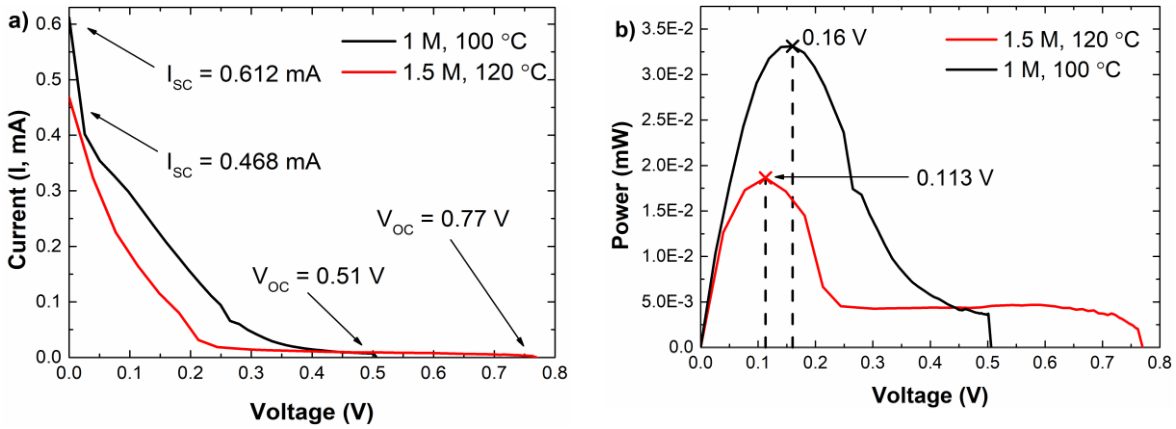

Figure 32: Solar cells a) IV and b) PV curves performances for $MAPbI_3$ thin films deposited over non-doped compact TiO_2 using 1M and 1.5 M solutions. TiO_2, $MAPbI_3$ and CuSCN depositions accomplished by, one-step spin coating of 6000 rpm with final annealing step of 500 °C for 30 min, two-step spin coating (1000 pm for 10 s and 6000 rpm for 20 s) dropping, in final seconds, 150 µL of chlorobenzene and annealing temperature of 100 °C and 120°C for 1 h and, one-step spin coating of 3000 rpm with final annealing step of 90 °C for 30 min, respectively.

Table 6: IV performance for best performance solar cells using doped and non-doped ETL layers.

Solar cells Parameters	V_{OC} (V)	J_{SC} (mA/cm²)	FF	R_P (kΩ)	R_S (kΩ)	PCE (%)
1 M 100 °C	0.516	7.65	0.106	0.12	13.18	0.414
1.5 M 120 °C	0.770	5.85	0.052	0.32	52.63	0.233

Once more, from the PV curves (Figure 32 b)) it is possible to observe the maximum voltage and therefore, the maximum current produced by the solar cells. In this way, using equation 1, 2 and 3 from Appendices, it is obtained a FF of 0.106 and 0.052 and a PCE of 0.414 % and 0.233 % for solar cells produced with 1 M and 1.5 M solution concentration, respectively.

Contrarily to the previous attempts, for these solar cells the results were obtained right after the contacts deposition. Besides having similar V_{OC}, it is noticeable a substantial current improvement, reaching close to 1 mA. However, the same bulk coverage results were obtained, which may be the explanation for the very low fill factor, due to the combination of low shunt resistance and high series resistance, according to Figure 34 from **section 1 of Appendices**. Other similar IV performances were measured for the same conditions and even for solar cells built over Li^+ doped compact TiO_2. However, despite the similar open circuit voltage, the measured current densities were significantly lower, as shown by Figure 43 from Appendices.

Since the ETL doping did not improve the solar cells performances, more solar cells were produced based on non-doped ETL. The results were, unfortunately, very similar to the previous obtained, with low current densities and very low fill factors. Generally, it was observed higher current densities for solar cells based on mesoporous TiO_2 ETL, since it improves the light absorption, and higher V_{OC} for the compact architecture. The optical, morphological and best electrical results are summarized in Figure 37 b) and c), Figure 39 and Figure 43 of Appendices.

Despite the ETL and HTL/perovskite interfaces and bulk morphologies, other factors may have a significant impact on the solar cells performance. The perovskite material is composed of many ionic bounds which means the presence of ions. The ionic motion and respective interfacial accumulation within the perovskite structure was proved, generating defects, which work as recombination centers and may also create an opposite internal electric field resulting in poor charge collection. [58]

Chapter V: Conclusions and Future Trends

This work aimed at the fabrication and optimization of all layers which constitute the simplest perovskite solar cell structure: ETL, Active layer and HTL. In this way, optical, structural, morphological and electrical characterization were performed. However, the main objective was the optimization, by changing the fabrication steps, of the active layer ($MAPbI_3$) in order to reach high morphological quality as well as structural and, thus, reach good solar cells performance.

In the first part of this work, the optimization of ETL and HTL layers results on high transparencies (≈ 90 % over glass and 70-90 % over FTO coated glass) and low parasitic absorption (close to 0 % over glass and ≈ 10 % over FTO coated glass) in the UV-Vis spectrum, which is desired, specifically for ETL layers since, before reaching the active layer, the light will pass through the glass-FTO-ETL. Between TiO_2 and ZnO, ZnO proved to be more transmissive over a bigger optical spectrum range and, as is discussed in literature it has a significant higher electron mobility, thus hinting to be a better candidate for ETL layer. Regarding CuSCN, despite the different process conditions, the final ones remain the same as the literature since it is deposited over the $MAPbI_3$ films, and higher rotation speeds and annealing temperatures could have a significant negative influence over $MAPbI_3$ films morphology, which, as discussed, is an important factor for solar cells performance.

In a second part, five fabrication steps were changed, using two different perovskite solutions concentrations, and studied their influence in $MAPbI_3$ absorption spectra and morphology, specifically on polycrystalline grain domain size and overall ETL surface coverage. Here, besides the way as the chlorobenzene/toluene is dropped in the final seconds of spin coating, the amount such reagents, substrate and solution temperature deposition and the substrate variation were the factors which mostly influenced the $MAPbI_3$ films morphology and uniformity. It was observed better morphologies for chlorobenzene/toluene amounts between 100 – 200 µl, substrate and solution temperature > 25 °C (for T > 25 °C, the temperature increase only affected the polycrystalline grain size), and for films deposited over mesoporous TiO_2 due to the better wettability. In compact TiO_2 and ZnO layers it required a UV treatment to improve the surface wettability and, thus, to produce a compact and uniform $MAPbI_3$ thin film. In addition, it was observed and proved the perovskite organic component degradation for films produced over ZnO films annealed at 200 °C and produced as described.

On the other hand, the annealing temperature and the DMF:DMSO ratio factors influenced mostly the perovskite crystallization. In this case, the annealing temperature revealed better results for 100 °C using 1 M solution and 120 °C using 1.5 M solution, showing mostly, for both cases, the presence of (110), (112), (202), (220), (310), (224) and (314) planes which is indicative of tetragonal phase. The DMF:DMSO ratio of 1:4, besides bad reagents dissolution, induced a non-uniform transparent brown films formation, which is indicative of a bad crystallization justifying the absorbance decrease and proving that DMSO works mostly as coordination reagent. Therefore, 4:1 (DMF:DMSO) ratio was maintained as well as the two-step spin coating of 1000 rpm for 10 s and 6000 rpm for 20 s since for higher rotations it showed total film degradation and, thus, very bad uniformities.

In a nutshell, the optimization of such layers allowed the choice of the better conditions to be applied on the final solar cell structure, summarized on Table 7 and Table 8:

Table 7: Final deposition conditions of ETL and HTL layers for complete solar cell structure fabrication with final thickness range.

Fabrication Conditions	**TiO_2**	**ZnO**	**CuSCN**
Rotation Speed	6000 rpm – 30 s	6000 rpm – 30 s	3000 rpm – 30 s
Depositions Number	1	1	1
Annealing temperature	500 °C - 30 min	500 ºC – 30 min	90 °C – 30 min
Final Thickness	30-40 nm	20-40 nm	80-100 nm

Table 8: Final deposition conditions of Perovskite layer for complete solar cell structure fabrication with final thickness range.

Perovskite Fabrication Conditions	**Annealing temperature**	**Hot casting temperature**	**DMF:DMSO**	**Chlorobenzene**	**Final Thickness**
1 M	100 °C	70 °C	4:1	100 - 150 µL	400-500 nm
1.5 M	120 °C	70 °C	4:1	100 - 150 µL	600-700 nm

Throughout this study, polycrystalline grain domains in the micrometer range were obtained, which is remarkable since all perovskite films were produced without any ambient controlled condition. However, as Figure 30 from section 3 of Results and Discussion shows, poor bulk morphologic quality was obtained, especially for films produced using 1 M precursor solution over compact TiO_2, which may be the major cause for the bad solar cells fill factors. However, using 1M solution produced thinner films which is better considering the charge diffusion length.

Regarding overall solar cells performances, it was obtained very low current densities and fill factors mostly due to the very high series resistances and very low shunt resistances which are the origin of very low efficiencies. Despite that, good open circuit voltages and very high absorbances, close to 90 %, were obtained.

As future trends, for further morphology improvements, the perovskite thin films fabrication in controlled ambient conditions as low humidity percentage in air was reported and used by most of researchers. Recent studies reported also a good morphology improvement using $HPbI_3$ as a reagent for perovskite precursor solution, which appears to be promising for further improvements. [59] Besides that, higher substrates temperatures for hot casting method may be tested in order to study their influence on polycrystalline grains size.

The ionic feature of perovskite semiconductors may be a crucial factor for solar cells behavior, especially, for current collection as already discussed. In this way, an impedance spectroscopy study may be important to further understand other mechanisms which may influence the charge collection on electrodes. Also, Hall effect measurements, especially in ETL and HTL, are important since the electrical properties of such layers are crucial for a good charge collection and solar cells performances.

As discussed earlier, ZnO proved to have better optical and electrical properties than TiO_2. In this way, perovskite deposition over ZnO annealed at higher temperatures (≈ 500 °C) using the simple described solution must be tested and, if possible, compare its influence on IV solar cells performance with the usual TiO_2.

Finally, this work objective was to find the best condition for $MAPbI_3$ growth optimizing also the other layers. However, changing the halide or cation composition is possible to tune perovskite properties and, therefore, the deposition conditions may be different for each composition. As an example, it is known that $MAPbBr_3$ has a higher band gap, useful for tandem cells, and higher stabilities. In this way, the best deposition condition for each single halide or cation composition and, next, for mixed halide or cation composition may be a very useful and interesting study twoards higher efficiencies and, therefore, towards a better use of solar energy.

References

[1] M.-E. Ragoussi and T. Torres, “New generation solar cells: concepts, trends and perspectives,” *Chem. Commun.*, vol. 51, no. 19, pp. 3957–3972, 2015.

[2] W. J. Potscavage Jr, “Physics and engineering of organic solar cells,” Georgia Institute of Technology, 2010.

[3] D. Gaspar, “Desenvolvimento de células solares de Si nano-estruturado para aplicação em azulejos solares,” FCT-UNL, 2010.

[4] A. Polman, M. Knight, E. C. Garnett, B. Ehrler, and W. C. Sinke, “Photovoltaic materials: Present efficiencies and future challenges,” *Science.*, vol. 352, no. 6283, p. aad4424-1-aad4424-10, Apr. 2016.

[5] H. A. Atwater and A. Polman, “Plasmonics for improved photovoltaic devices,” *Nat. Mater.*, vol. 9, no. 10, pp. 865–865, Oct. 2010.

[6] M. Saliba *et al.*, “Cesium-containing triple cation perovskite solar cells: improved stability, reproducibility and high efficiency,” *Energy Environ. Sci.*, vol. 9, no. 6, pp. 1989–1997, 2016.

[7] N. J. Jeon, J. H. Noh, Y. C. Kim, W. S. Yang, S. Ryu, and S. Il Seok, “Solvent engineering for high-performance inorganic–organic hybrid perovskite solar cells,” *Nat. Mater.*, vol. 13, no. 9, pp. 897–903, Jul. 2014.

[8] W. Zhang, G. E. Eperon, and H. J. Snaith, “Metal halide perovskites for energy applications,” *Nat. Energy*, vol. 1, no. 6, p. 16048, May 2016.

[9] G. E. Eperon, V. M. Burlakov, P. Docampo, A. Goriely, and H. J. Snaith, “Morphological Control for High Performance, Solution-Processed Planar Heterojunction Perovskite Solar Cells,” *Adv. Funct. Mater.*, vol. 24, no. 1, pp. 151–157, Jan. 2014.

[10] M. Ye, X. Hong, F. Zhang, and X. Liu, “Recent advancements in perovskite solar cells: flexibility, stability and large scale,” *J. Mater. Chem. A*, vol. 4, no. 18, pp. 6755–6771, 2016.

[11] F. Hao, C. C. Stoumpos, D. H. Cao, R. P. H. Chang, and M. G. Kanatzidis, “Lead-free solid-state organic–inorganic halide perovskite solar cells,” *Nat. Photonics*, vol. 8, no. 6, pp. 489–494, May 2014.

[12] H. S. Jung and N.-G. Park, “Perovskite Solar Cells: From Materials to Devices,” *Small*, vol. 11, no. 1, pp. 10–25, Jan. 2015.

[13] T. Baikie *et al.*, “Synthesis and crystal chemistry of the hybrid perovskite $(CH_3NH_3)PbI_3$ for solid-state sensitised solar cell applications,” *J. Mater. Chem. A*, vol. 1, no. 18, p. 5628, 2013.

[14] M. Grätzel, “The light and shade of perovskite solar cells,” *Nat. Mater.*, vol. 13, no. 9, pp. 838–842, Aug. 2014.

[15] M. A. Green, A. Ho-Baillie, and H. J. Snaith, “The emergence of perovskite solar cells,” *Nat. Photonics*, vol. 8, no. 7, pp. 506–514, Jun. 2014.

[16] J. Burschka *et al.*, “Sequential deposition as a route to high-performance perovskite-sensitized solar cells,” *Nature*, vol. 499, no. 7458, pp. 316–319, Jul. 2013.

[17] C.-H. Chiang, Z.-L. Tseng, and C.-G. Wu, “Planar heterojunction perovskite/$PC_{71}BM$ solar cells with enhanced open-circuit voltage via a (2/1)-step spin-coating process,” *J. Mater. Chem. A*, vol. 2, no. 38, pp. 15897–15903, 2014.

[18] Q. Chen *et al.*, “Planar Heterojunction Perovskite Solar Cells via Vapor-Assisted Solution Process,” *J. Am. Chem. Soc.*, vol. 136, no. 2, pp. 622–625, Jan. 2014.

[19] B. R. Sutherland *et al.*, “Perovskite Thin Films via Atomic Layer Deposition,” *Adv. Mater.*, vol. 27, no. 1, pp. 53–58, Jan. 2015.

[20] D. Liu and T. L. Kelly, “Perovskite solar cells with a planar heterojunction structure prepared using room-temperature solution processing techniques,” *Nat. Photonics*, vol. 8, no. 2, pp. 133–138, Dec. 2013.

[21] Z. Wei, H. Chen, K. Yan, and S. Yang, “Inkjet Printing and Instant Chemical Transformation of a CH 3 NH 3 PbI 3 /Nanocarbon Electrode and Interface for Planar Perovskite Solar Cells,” *Angew. Chemie*, vol. 126, no. 48, pp. 13455–13459, Nov. 2014.

[22] J.-H. Im, I.-H. Jang, N. Pellet, M. Grätzel, and N.-G. Park, “Growth of $CH_3NH_3PbI_3$ cuboids with controlled size for high-efficiency perovskite solar cells,” *Nat. Nanotechnol.*, vol. 9, no. 11, pp. 927–932, Aug. 2014.

[23] A. T. Barrows, A. J. Pearson, C. K. Kwak, A. D. F. Dunbar, A. R. Buckley, and D. G. Lidzey, “Efficient planar heterojunction mixed-halide perovskite solar cells deposited via spray-deposition,” *Energy Environ. Sci.*, vol. 7, no. 9, pp. 2944–2950, 2014.

[24] A. Dualeh, N. Tétreault, T. Moehl, P. Gao, M. K. Nazeeruddin, and M. Grätzel, “Effect of Annealing Temperature on Film Morphology of Organic-Inorganic Hybrid Pervoskite Solid-State Solar Cells,” *Adv. Funct. Mater.*, vol. 24, no. 21, pp. 3250–3258, Jun. 2014.

[25] M. Xiao *et al.*, “A fast deposition-crystallization procedure for highly efficient lead iodide perovskite thin-film solar cells.,” *Angew. Chem. Int. Ed. Engl.*, vol. 53, no. 37, pp. 9898–903, Sep. 2014.

[26] W. Nie *et al.*, “High-efficiency solution-processed perovskite solar cells with millimeter-scale grains,” *Science.*, vol. 347, no. 6221, pp. 522–525, Jan. 2015.

[27] B. Cai, W.-H. Zhang, and J. Qiu, “Solvent engineering of spin-coating solutions for planar-structured high-efficiency perovskite solar cells,” *Chinese J. Catal.*, vol. 36, no. 8, pp. 1183–1190, Aug. 2015.

[28] B. Conings *et al.*, “Intrinsic Thermal Instability of Methylammonium Lead Trihalide Perovskite,” *Adv. Energy Mater.*, vol. 5, no. 15, pp. 1–8, Aug. 2015.

[29] H. Tsai *et al.*, “Effect of Precursor Solution Aging on the Crystallinity and Photovoltaic Performance of Perovskite Solar Cells,” *Adv. Energy Mater.*, vol. 7, no. 11, pp. 1–9, Jun. 2017.

[30] S. D. Stranks *et al.*, “Electron-Hole Diffusion Lengths Exceeding 1 Micrometer in an Organometal Trihalide Perovskite Absorber,” *Science.*, vol. 342, no. 6156, pp. 341–344, Oct. 2013.

[31] V. Zardetto *et al.*, “Atomic layer deposition for perovskite solar cells: research status, opportunities and challenges,” *Sustain. Energy Fuels*, vol. 1, no. 1, pp. 30–55, 2017.

[32] J. H. Park *et al.*, “Efficient CH 3 NH 3 PbI 3 Perovskite Solar Cells Employing Nanostructured p-Type NiO Electrode Formed by a Pulsed Laser Deposition,” *Adv. Mater.*, vol. 27, no. 27, pp. 4013–4019, Jul. 2015.

[33] B. Conings, L. Baeten, C. De Dobbelaere, J. D’Haen, J. Manca, and H.-G. Boyen, “Perovskite-Based Hybrid Solar Cells Exceeding 10% Efficiency with High Reproducibility Using a Thin Film Sandwich Approach,” *Adv. Mater.*, vol. 26, no. 13, pp. 2041–2046, Apr. 2014.

[34] J. H. Heo, D. H. Song, and S. H. Im, “Planar $CH_3NH_3PbBr_3$ Hybrid Solar Cells with 10.4% Power Conversion Efficiency, Fabricated by Controlled Crystallization in the Spin-Coating Process,” *Adv. Mater.*, vol. 26, no. 48, pp. 8179–8183, Dec. 2014.

[35] J. You *et al.*, “Improved air stability of perovskite solar cells via solution-processed metal oxide transport layers,” *Nat. Nanotechnol.*, vol. 11, no. 1, pp. 75–81, Oct. 2015.

[36] Y. Sun, J. H. Seo, C. J. Takacs, J. Seifter, and A. J. Heeger, “Inverted Polymer Solar Cells Integrated with a Low-Temperature-Annealed Sol-Gel-Derived ZnO Film as an Electron Transport Layer,” *Adv. Mater.*, vol. 23, no. 14, pp. 1679–1683, Apr. 2011.

[37] R. E. Beal *et al.*, “Cesium Lead Halide Perovskites with Improved Stability for Tandem Solar Cells,” *J. Phys. Chem. Lett.*, vol. 7, no. 5, pp. 746–751, Mar. 2016.

[38] E. Edri, S. Kirmayer, D. Cahen, and G. Hodes, “High Open-Circuit Voltage Solar Cells Based on Organic-Inorganic Lead Bromide Perovskite.,” *J. Phys. Chem. Lett.*, vol. 4, no. 6, pp. 897–902, Mar. 2013.

[39] E. Chikoidze, M. Nolan, M. Modreanu, V. Sallet, and P. Galtier, “Effect of chlorine doping on electrical and optical properties of ZnO thin films,” *Thin Solid Films*, vol. 516, no. 22, pp. 8146–8149, Sep. 2008.

[40] Y. Mi and Y. Weng, “Band Alignment and Controllable Electron Migration between Rutile and Anatase TiO_2.,” *Sci. Rep.*, vol. 5, no. 1, pp. 1–10, Jul. 2015.

[41] J. Duan, Q. Xiong, H. Wang, J. Zhang, and J. Hu, “ZnO nanostructures for efficient perovskite solar cells,” *J. Mater. Sci. Mater. Electron.*, vol. 28, no. 1, pp. 60–66, Jan. 2017.

[42] Z. Song, S. C. Watthage, A. B. Phillips, and M. J. Heben, “Pathways twoard high-performance perovskite solar cells: review of recent advances in organo-metal halide perovskites for photovoltaic applications,” *J. Photonics Energy*, vol. 6, no. 2, pp. 22001 (1-23), Apr. 2016.

[43] M. Jung *et al.*, “Thermal Stability of CuSCN Hole Conductor-Based Perovskite Solar Cells,” *ChemSusChem*, vol. 9, no. 18, pp. 2592–2596, Sep. 2016.

[44] P. Qin *et al.*, “Inorganic hole conductor-based lead halide perovskite solar cells with 12.4%

conversion efficiency," *Nat. Commun.*, vol. 5, pp. 1–6, May 2014.

[45] M. Kim *et al.*, "Band-Tail Transport of CuSCN: Origin of Hole Extraction Enhancement in Organic Photovoltaics," *J. Phys. Chem. Lett.*, vol. 7, no. 14, pp. 2856–2861, Jul. 2016.

[46] S. Ye *et al.*, "CuSCN-Based Inverted Planar Perovskite Solar Cell with an Average PCE of 15.6%," *Nano Lett.*, vol. 15, no. 6, pp. 3723–3728, Jun. 2015.

[47] F. Giordano *et al.*, "Enhanced electronic properties in mesoporous TiO_2 via lithium doping for high-efficiency perovskite solar cells," *Nat. Commun.*, vol. 7, p. 10379, Jan. 2016.

[48] K. Zhao, R. Munir, B. Yan, Y. Yang, T.-S. Kim, and A. Amassian, "Solution-processed inorganic copper(I) thiocyanate (CuSCN) hole transporting layers for efficient p–i–n perovskite solar cells," *J. Mater. Chem. A*, vol. 3, no. 41, pp. 20554–20559, 2015.

[49] D. Dam Le, T. M. Dung Dang, V. Thang Chau, and M. Chien Dang, "The fabrication of visible light responsive Ag-SiO_2 co-doped TiO_2 thin films by the sol–gel method," *Adv. Nat. Sci. Nanosci. Nanotechnol.*, vol. 1, no. 1, p. 15007, Mar. 2010.

[50] T. M. Dung Dang, D. Dam Le, V. Thang Chau, and M. Chien Dang, "Visible-light photocatalytic activity of N/SiO_2 –TiO_2 thin films on glass," *Adv. Nat. Sci. Nanosci. Nanotechnol.*, vol. 1, no. 1, p. 15004, Mar. 2010.

[51] J. W. Jung, C.-C. Chueh, and A. K. Y. Jen, "High-Performance Semitransparent Perovskite Solar Cells with 10% Power Conversion Efficiency and 25% Average Visible Transmittance Based on Transparent CuSCN as the Hole-Transporting Material," *Adv. Energy Mater.*, vol. 5, no. 17, p. 1500486 (1-7), Sep. 2015.

[52] J. Ding, Y. Li, H. Hu, L. Bai, S. Zhang, and N. Yuan, "The influence of anatase-rutile mixed phase and ZnO blocking layer on dye-sensitized solar cells based on TiO_2 nanofiberphotoanodes," *Nanoscale Res. Lett.*, vol. 8, no. 1, pp. 1–9, 2013.

[53] M. Smirnov, C. Baban, and G. I. Rusu, "Structural and optical characteristics of spin-coated ZnO thin films," *Appl. Surf. Sci.*, vol. 256, no. 8, pp. 2405–2408, 2010.

[54] M. Mulato, I. Chambouleyron, E. G. Birgin, and J. M. Martínez, "Determination of thickness and optical constants of amorphous silicon films from transmittance data," *Appl. Phys. Lett.*, vol. 77, no. 14, pp. 2133–2135, Oct. 2000.

[55] Y. Zhao and K. Zhu, "Charge Transport and Recombination in Perovskite (CH_3NH_3)PbI_3 Sensitized TiO_2 Solar Cells," *J. Phys. Chem. Lett.*, vol. 4, no. 17, pp. 2880–2884, 2013.

[56] G. Rajendra Kumar *et al.*, "Phase transition kinetics and surface binding states of methylammonium lead iodide perovskite," *Phys. Chem. Chem. Phys.*, vol. 18, no. 10, pp. 7284–7292, 2016.

[57] B. Conings *et al.*, "Intrinsic Thermal Instability of Methylammonium Lead Trihalide Perovskite," *Adv. Energy Mater.*, vol. 5, no. 15, pp. 1500477 (1–8), Aug. 2015.

[58] N. K. Elumalai and A. Uddin, "Hysteresis in organic-inorganic hybrid perovskite solar cells," *ELSEVIER*, vol. 157, pp. 476–509, Dec. 2016.

[59] F. Wang, H. Yu, H. Xu, and N. Zhao, "$HPbI_3$: A New Precursor Compound for Highly Efficient Solution-Processed Perovskite Solar Cells," *Adv. Funct. Mater.*, vol. 25, no. 7, pp. 1120–1126, Feb. 2015.

[60] P. Hernday, "Field Applications for I-V Curve Tracers," 2011. [Online]. Available: http://solarprofessional.com/articles/design-installation/field-applications-for-i-v-curve-tracers/page/0/3#.WcWOcsiGPIV. [Accessed: 22-Sep-2017].

[61] National Instruments, "Part II – Photovoltaic Cell I-V Characterization Theory and LabVIEW Analysis Code," 2012. [Online]. Available: http://www.ni.com/white-paper/7230/en/#top. [Accessed: 23-Sep-2017].

[62] P. Vivo *et al.*, "Influence of TiO_2 compact layer precursor on the performance of perovskite solar cells," *Org. Electron.*, vol. 41, pp. 287–293, Feb. 2017.

[63] N. Sakai *et al.*, "The mechanism of toluene-assisted crystallization of organic–inorganic perovskites for highly efficient solar cells," *J. Mater. Chem. A*, vol. 4, no. 12, pp. 4464–4471, 2016.

Appendices

1. Solar Cell Parameters Equations

In this section is explained the calculation solar cells parameters through the IV and PV curves and presented the main equations used in section 3 of Results and Discussion. Besides, Figure 34 shows the influence of series and shunt resistances, R_S and R_P (or R_{SH}), on IV solar cells curves and specially on Fill Factor.

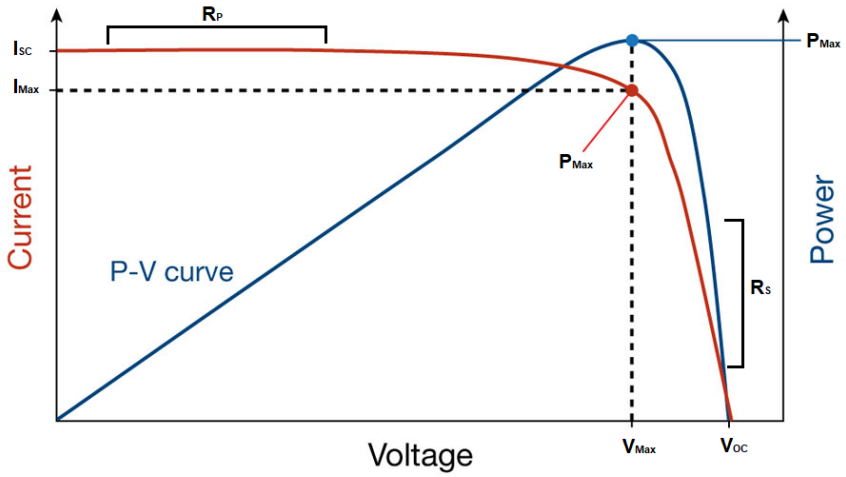

Figure 33: IV solar cell curve illustration for parameters calculation. [60]

- I_{SC}, short circuit current, obtained at V = 0 V;
- V_{OC}, open circuit voltage, obtained at I = 0V;
- I_{mp} and V_{mp}, maximum current and voltage respectively, obtained by IV curve, illustrated by Figure 33;
- R_s and R_P, series and parallel resistance, respectively, obtained by (IV curve slope)$^{-1}$ in region showed by Figure 33;
- P_{Max}, maximum generated power:

$$P_{Max} = I_{mp} \times V_{mp} \quad (1)$$

- FF, fil factor, proximity of IV curve to a square, obtained by:

$$FF = \frac{I_{mp} \times V_{mp}}{I_{SC} \times V_{OC}} \quad (2)$$

- η, Efficiency, also denominated as PCE, is the ratio between P_{Max} and P_{light}:

$$\eta = \frac{P_{Max}}{P_{light}} \times 100\ \% \quad (3)$$

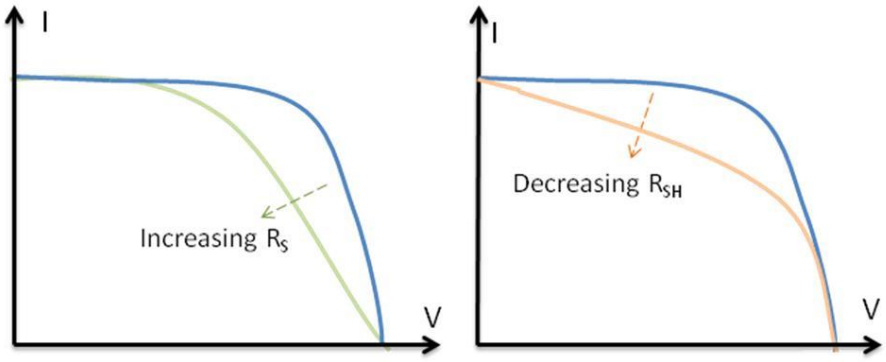

Figure 34: Influence of series (left) and shunt (right) resistances, R_S and R_P (or R_{SH}), on IV solar cells performances. The series resistance increase and the shunt resistance decrease may also induce the I_{SC} and V_{OC} decreases, respectively. [61]

2. Materials

Table 9:List of reagents and respective abbreviation, purity, CAS and company.

Reagent	Abbreviation	Purity	CAS	Company
Absolute Ethanol	EtOH	99.99 %	64-17-5	*Fisher Chemical*
Acetonitrile	-	99.5 %	75-05-8	Riedel-de Haën
Copper(I) Thiocyanate	CuSCN	96 %	1111-67-7	*Alfa Aesar*
Di-n-propyl Sulfide	-	98 %	111-47-7	*Alfa Aesar*
Dimethylformamide	DMF	99.8 %	68-12-2	*Panreac*
Dimethyl Sulfoxide	DMSO	99.9 %	67-68-5	*Fisher Chemical*
Ethanolamine	-	99 %	141-43-5	Riedel-de Haën
Hydrochloric Acid	HCL	37 %	7647-01-0	*SIGMA ALDRICH*
Lithium salt	Li-TFSI	-	90076-65-6	*SIGMA ALDRICH*
Methylammonium Iodide	MAI	98 %	14965-49-2	*SIGMA ALDRICH*
Lead Iodide	PbI_2	99 %	10101-63-0	*ACROS ORGANIC*
Colloidal TiO_2 Paste (22 nm)	-	-	-	*SIGMA ALDRICH*
Titanium(IV) Isopropoxide	TTIP	97 %	546-68-9	*SIGMA ALDRICH*
Zinc Acetate Dihydrate	ZAD	99-102%	5970-45-6	*SIGMA ALDRICH*
2-methoxyethanol	-	99.8%	109-86-4	*SIGMA ALDRICH*

3. Solutions Preparation

This section presents the recipes for the solutions preparation (e.g. reagents, stirring time, temperature) used in the Experimental section.

3.1. ETL and Li^+ doping precursor solutions

The fours precursor solutions needed for ETL fabrication were prepared using the following materials: a liquid reagent of Titanium(IV) Isopropoxide (TTPI), absolute ethanol (EtOH), Hydrochloric acid (HCL), a 22 nm TiO_2 particle paste, zinc acetate dihydrate (ZAD - $Zn(CH_2COO)_2 .2H_2O$), 2-methoxyethanol, ethanolamine and Li-TFSI (lithium slat).

1. For the TiO_2 compact layer, a solution consisting of 17.5 µL of HCl in 1.25 mL of EtOH was added, by dropwise, to a solution of 175 µL of TTIP in 1.25 mL of EtOH and stirred, at least, for 10 min. [62, 63]
2. TiO_2 Mesoporous precursor solution was prepared diluting a 22 nm TiO_2 particle paste in EtOH with a concentration of 150 mg/mL and stirred for 10 min.
3. The solution which was used on TiO_2 doping was prepared diluting Li-TFSI in acetonitrile with a concentration of 0.1 M. [47]
4. The ZnO precursor solution was developed stirring, at least for 12 h (for the hydrolysis reaction), a solution of 1 g of ZAD in 280 µL of ethanolamine and 10 mL of 2-methoxyethanol, as described elsewhere [36].

3.2. HTL precursor solution

The precursor solution for HTL fabrication was prepared using a Copper(I) Thiocyanate (CuSCN) powder dissolved in Di-n-propyl sulfide (98%) with a concentration of 15 mg/mL and stirred for 48 h, as described elsewhere [48]

3.3. Perovskite precursor solution

The materials used to perform the perovskite precursor solutions was Methylammonium Iodide (MAI), Lead Iodide (PbI_2) powders. As solvent was used a mix of dimethylformamide (DMF) and dimethyl sulfoxide (DMSO), with ratios (DMF:DMSO) of 4:1 and 1:4.

These solutions with concentrations of 1M and 1.5 M were stirred at 70 °C until it turned into homogeneous yellow solution. Table 10 presents the quantities used for 1 ml of precursor solution for each concentration:

Table 10: Reagent molarity for 1 M and 1.5 M precursor solutions.

Reagent quantity (mmol)	MAI	PbI_2
$MAPbI_3$ (1 M)	1	1
$MAPbI_3$ (1.5 M)	1.5	1.5

4. Optical Analysis

This section aims manly to study the optical behavior reproducibility of ETL and HTL deposited over non-coated and FTO-coated glass, as well as of the full solar cells structure without the Au contacts. Besides, it is presented also, for the TiO_2 films, the analytically-simulated direct transmittance fitting curves for thickness determination and the annealing time influence on the absorbance spectra of perovskite thin films prepared using 1.5 M precursor solution concentration (section 2.5 of Results and Discussion).

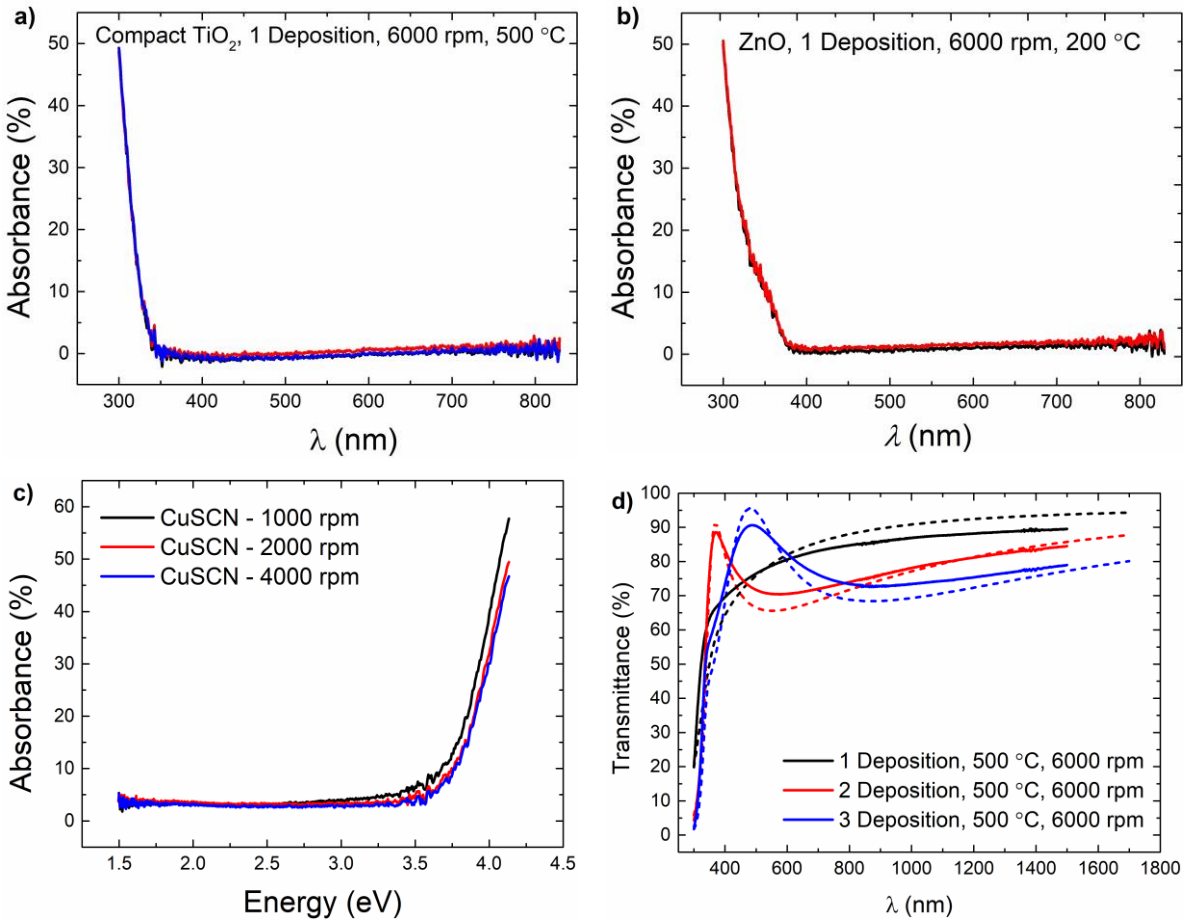

Figure 35: Absorbance spectra reproducibility of a) TiO_2, b) ZnO, c) CuSCN and d) measured (solid lines) vs simulated Transmittance curves (short dash curves) for compact TiO_2 thickness determination (setting in program 31 nm for 1 Deposition, 62 nm for 2 Depositions and 96 nm for 3 depositions) deposited over non-coated glass.

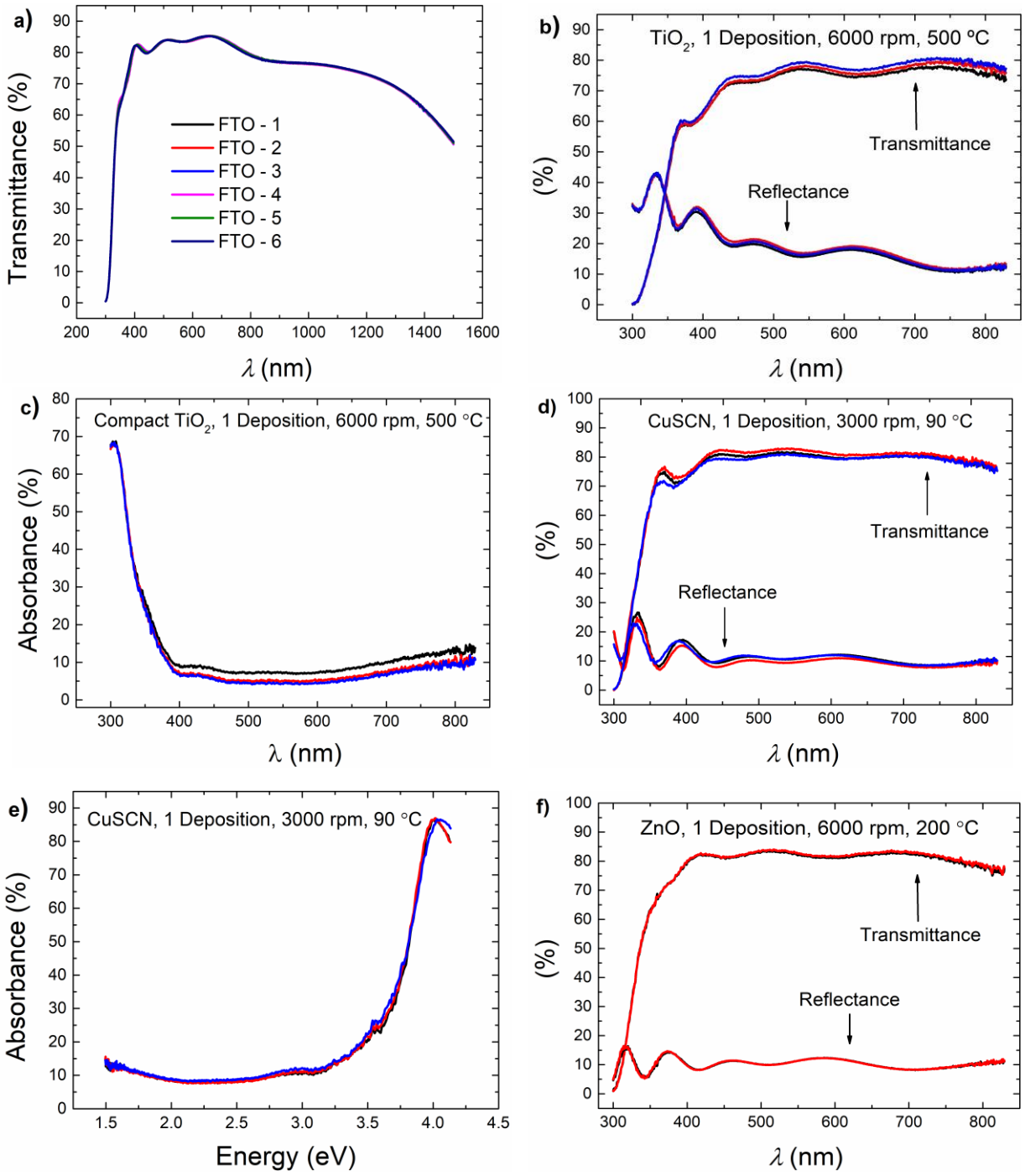
a)
Transmittance (%)
FTO - 1
FTO - 2
FTO - 3
FTO - 4
FTO - 5
FTO - 6
λ (nm)
b)
TiO2, 1 Deposition, 6000 rpm, 500 ºC
Transmittance
Reflectance
(%)
λ (nm)
c)
Compact TiO2, 1 Deposition, 6000 rpm, 500 °C
Absorbance (%)
λ (nm)
d)
CuSCN, 1 Deposition, 3000 rpm, 90 °C
Transmittance
Reflectance
(%)
λ (nm)
e)
CuSCN, 1 Deposition, 3000 rpm, 90 °C
Absorbance (%)
Energy (eV)
f)
ZnO, 1 Deposition, 6000 rpm, 200 °C
Transmittance
Reflectance
(%)
λ (nm)

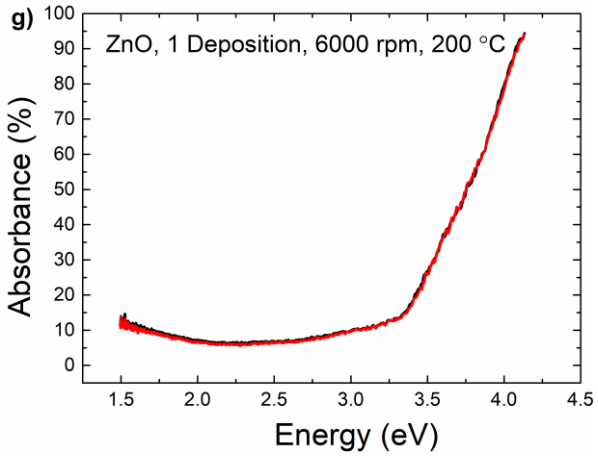

Figure 36: Optical behavior reproducibility of a) FTO coated glass, b) and c) compact TiO_2, d) and e) compact CuSCN, f) and g) compact ZnO deposited under final chosen conditions over FTO coated glass.

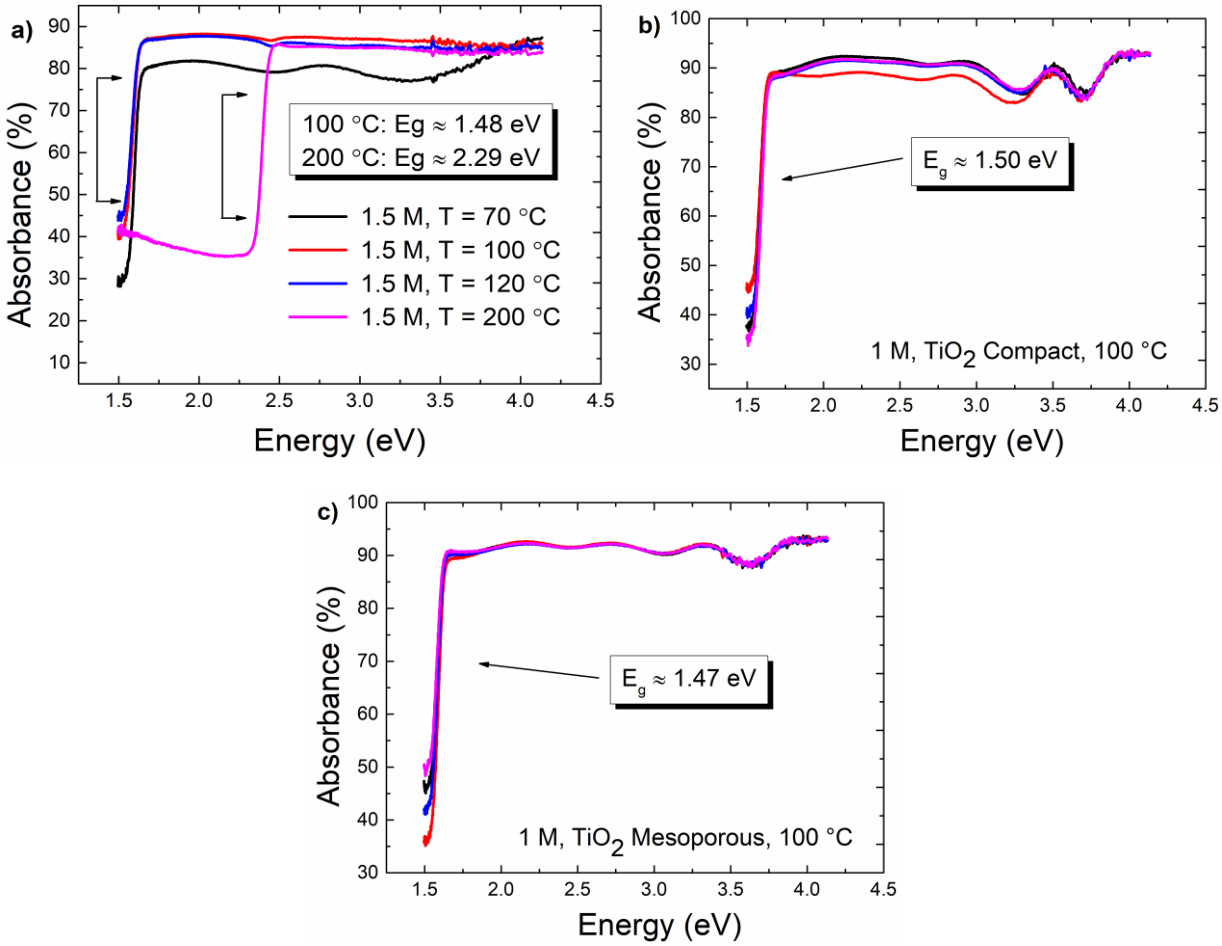

Figure 37: Absorbance spectra of a) $MAPbI_3$ annealed at distinct temperatures using 1.5 M solution, b) and c) full solar cells structures built over compact and mesoporous TiO_2, respectively. The band gap was obtained by making a linear fit in the drop zone of the curve and obtaining the intersection point with the X-Axis using the line equation (Y = mX + b).

5. SEM Analysis

Figure 38 and Figure 39 present the SEM analysis showing the polycrystalline films, with distinct grain size distribution, produced in section 2.5 and section 3, respectively, of Results and Discussion.

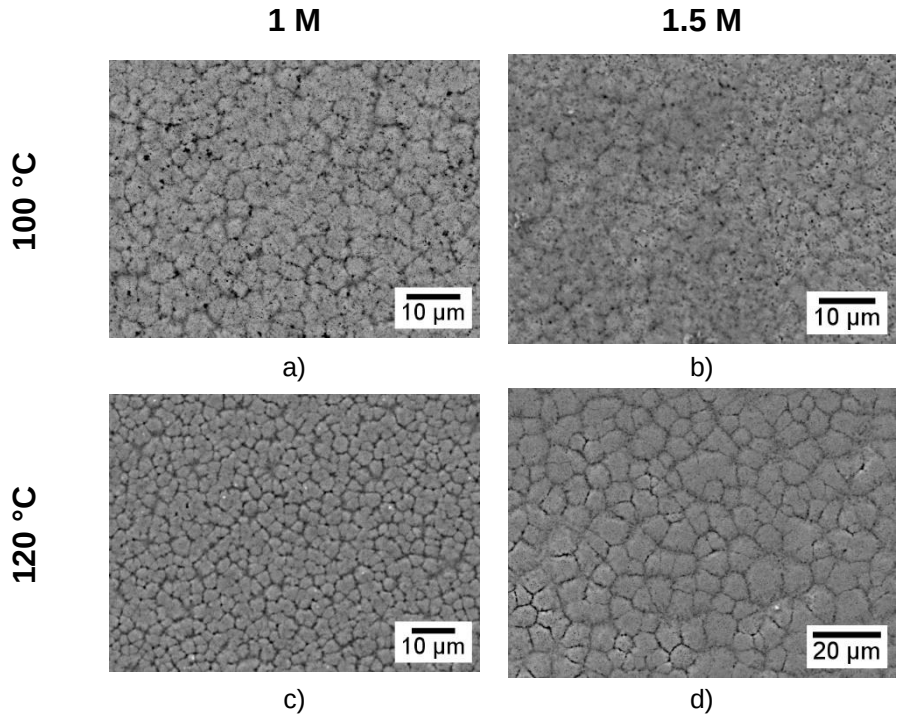

Figure 38: Influence of annealing temperature on $MAPbI_3$ thin films morphology and grain size, deposited over mesoporous TiO_2. Films deposited with solutions and substrates at 70 °C by two-step program spin coating, 1000 rpm for 10 s and 6000 rpm for 20 s, dropping 150 µL of chlorobenzene in final seconds, using 1 M, a), c), and 1.5 M, b), d), solutions. Annealing step accomplished for 1 h for each temperature.

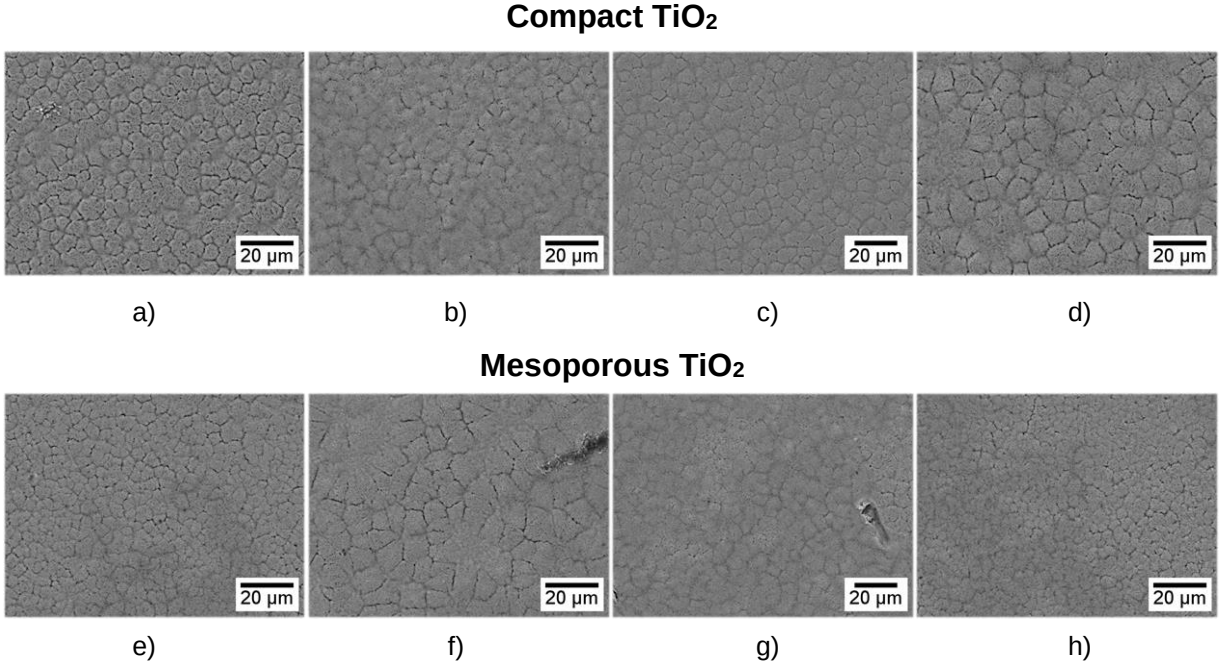

Figure 39: $MAPbI_3$ thin films morphology and grain size, deposited over a)-d) compact and e)-h) mesoporous TiO_2. Films deposited with solutions and substrates at 70 °C by two-step program spin coating, 1000 rpm for 10 s and 6000 rpm for 20 s, dropping 150 µL of chlorobenzene in final seconds, using 1 M solution concentration. Annealing step accomplished at 100 °C for 1 h

6. Polycrystalline Grain Domain Size

Table 11 and Table 12 represent the polycrystalline grain size of films produced in section 2.5 and section 3, respectively, of Results and Discussion.

Table 11: $MAPbI_3$ polycrystalline grain domain size deposited over mesoporous TiO_2 and annealed at distinct temperatures. Size determination based on an average of ten measurements per sample using CorelDRAW software.

Grain Size (µm)	**1 M**	**1.5 M**
100 °C	3.55 ± 0.54	-
120 °C	2.89 ± 0.46	6.87 ± 0.90

Table 12: $MAPbI_3$ polycrystalline grain domain size deposited over Li^+ doped and non-doped compact TiO_2 and Li^+ doped mesoporous TiO_2. Size determination based on an average of ten measurements per sample using CorelDRAW software.

Grain Size (µm)	***Compact TiO_2***	***Li^+ Doped Compact TiO_2***	***Li^+ Doped Mesoporous TiO_2***
1 M 100 °C	7.99 ± 1.41	5.71 ± 1.23	7.37 ± 1.55
1.5 M 120 °C	5.94 ± 0.78	9.72 ± 2.90	6.21 ± 1.23

7. EDS Analysis

The EDS analysis were performed on complete solar cell structures (without Au contacts), to prove the presence of all layers. These EDS spectra are part of section 3 of Results and Discussion results.

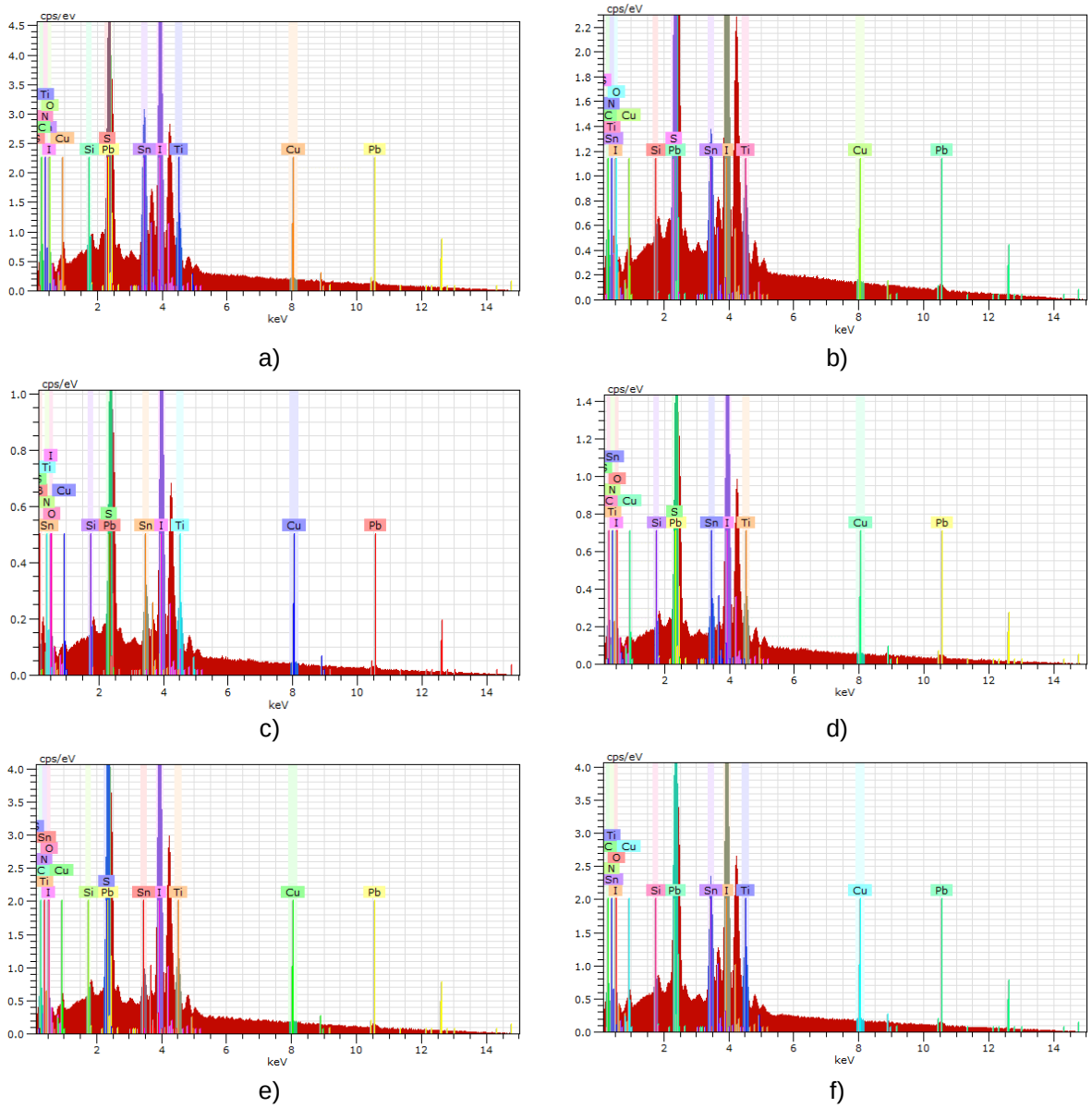

Figure 40: EDS analysis of $MAPbI_3$ thin films, deposited over Li^+ non-doped (a), b)) and doped compact (c), d)) and Li^+ doped mesoporous TiO_2 (e), f)). Films deposited with solutions and substrates at 70 °C by two-step program spin coating, 1000 rpm for 10 s and 6000 rpm for 20 s, dropping 150 µL of chlorobenzene in final seconds, using 1 M, a), c) and e), and 1.5 M, b), d) and f), solutions. Annealing step accomplished at 100 °C and 120 °C for 1 h for each temperature.

8. AFM Analysis

The 2D AFM analysis enabled the study of surface topography uniformity, being a complementary study to section 1.3 of Results and Discussion.

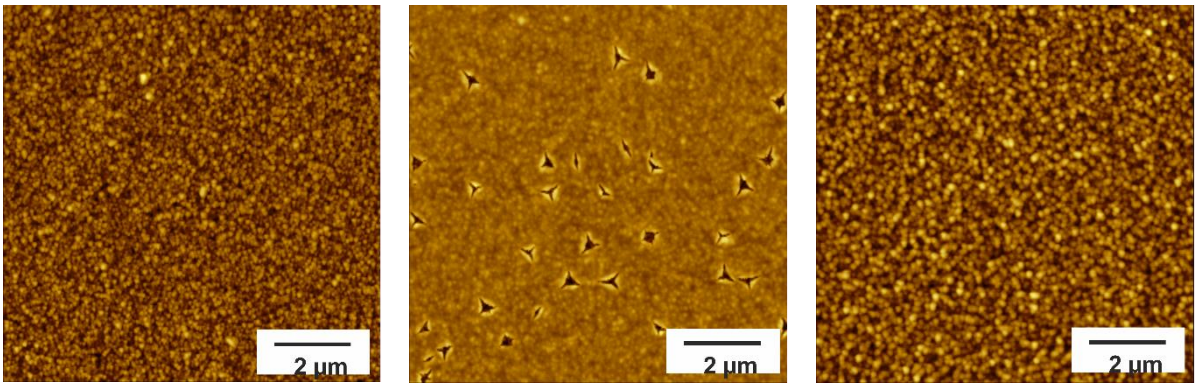

a) b) c)

Figure 41: AFM images of a) FTO coated glass, b) FTO coated glass with approximately 30 nm of TiO_2 and c) FTO coated glass with approximately 30 nm of ZnO, deposited with final defined conditions. Rms determination in data analysis software Gwyddion.

9. XRD Spectra

Here it was studied the perovskite phase depending on annealing temperature and precursor solution concentration. This is a complementary study from section 2.5 of Results and discussion.

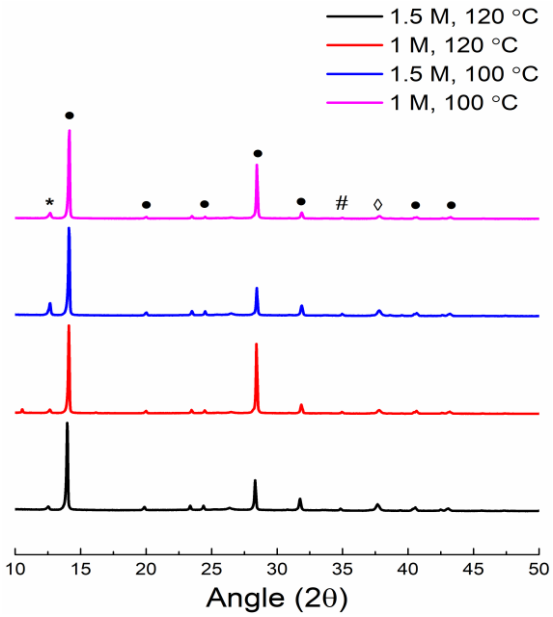

Figure 42: XRD analysis of $MAPbI_3$ thin films using 1 M and 1.5 M solutions, deposited over compact TiO_2, annealed at distinct temperatures. In XRD spectra, the tetragonal perovskite phase is identified by a full circle, the PbI_2 phase is identified by an asterisk and finally the CuSCN and FTO phases are identified with a cardinal and rhomb respectively.

10. IV Solar Cell Performances

This section presents some selected IV performance results of cells with lower efficiencies, mostly due to the lower currents and fill factors. In this way, this section is part of solar cell characterization (section 3 of Results and Discussion).

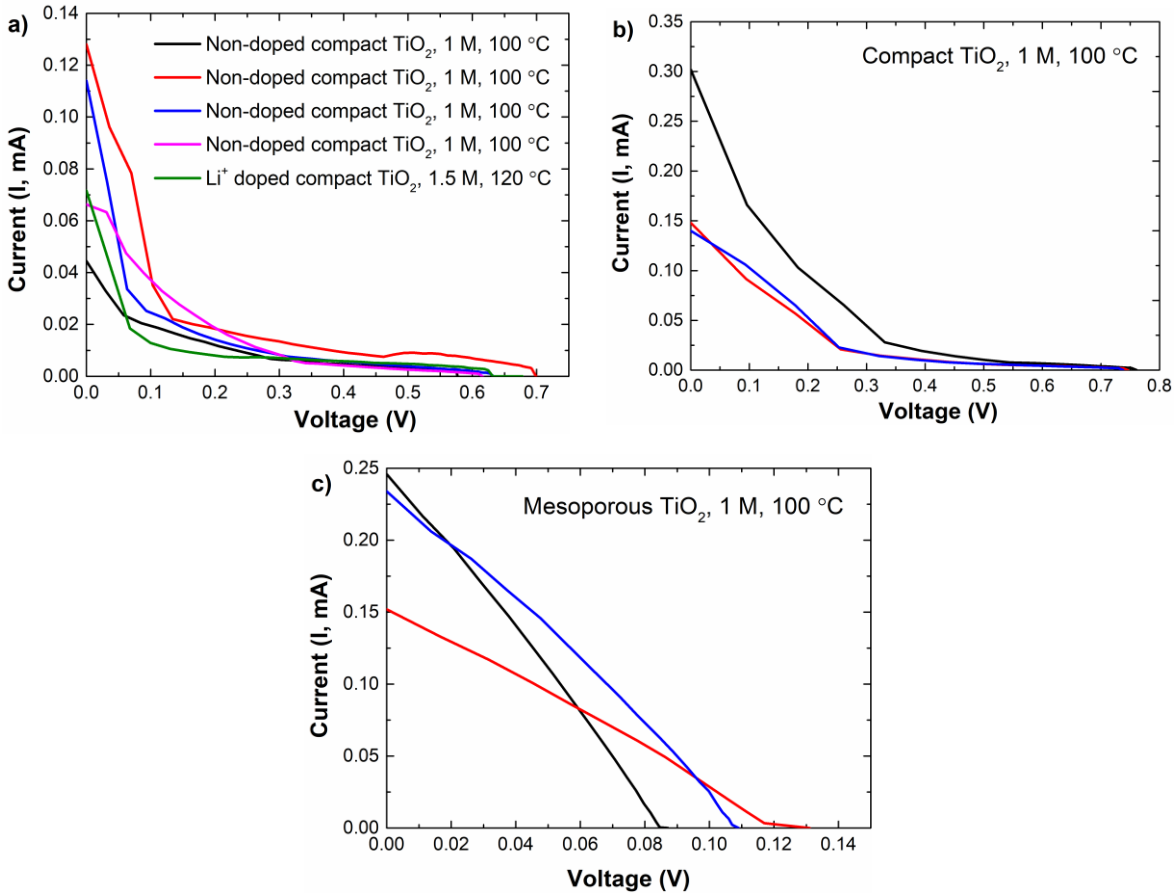

Figure 43: IV performances of solar cells built over a) doped and non-doped compact TiO_2, b) compact TiO_2 and c) mesoporous TiO_2. $MAPbI_3$ thin films deposited under chosen conditions as well as ETL and HTL layers.

11. Solar Cells Images

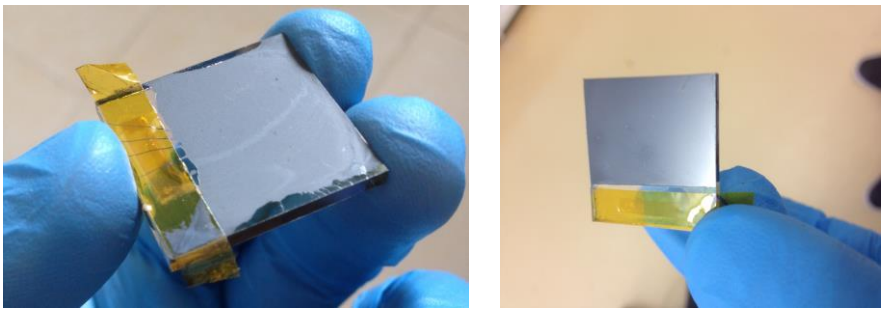

a) b)

Figure 44: $MAPbI_3$ thin film deposited over a) FTO substrate and b) compact TiO_2 with chosen conditions. Light-grey film color of figure a) means the formation of multiple pinholes.

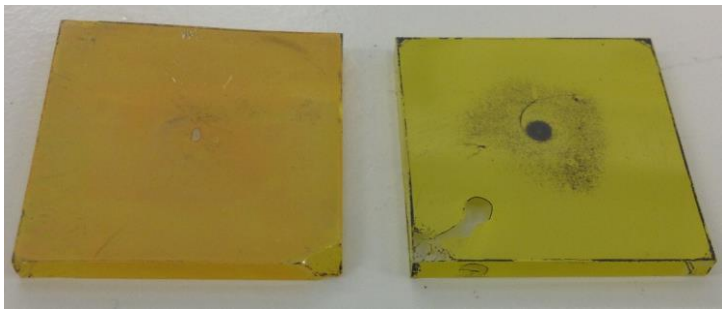

Figure 45: $MAPbI_3$ thin film deposited over compact TiO_2 substrate with chosen conditions using 1 M (left) and 1.5 M (right) solution concentration, annealed at a temperature of 200 ºC for 1h.

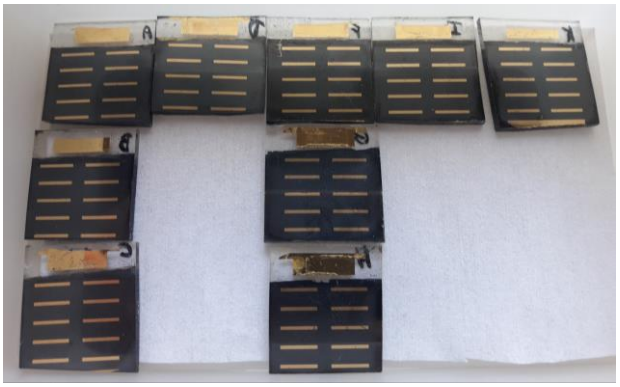

Figure 46: Solar cells batch of perovskite films deposited over compact and mesoporous TiO_2 ETL.

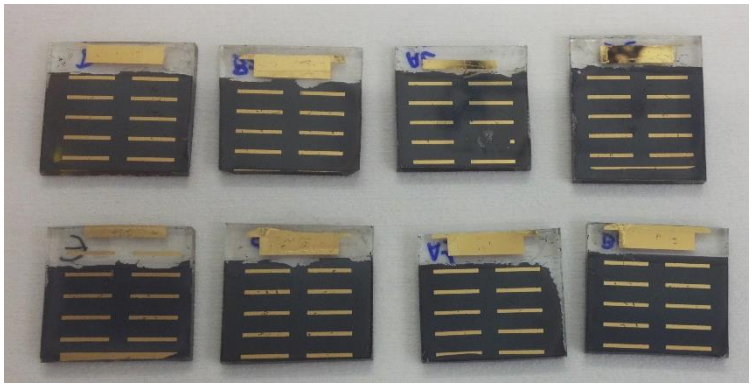

Figure 47: Solar cells batch of perovskite films deposited over compact and mesoporous TiO_2 ETL using 1 M and 1.5 M solutions concentration.